Journal of Fluids and Structures 137 (2025) 104381

Contents lists available at ScienceDirect

Journal of Fluids and Structures

journal homepage: www.elsevier.com/locate/jfs

Modelling unsteady hydrodynamic gust loading on tidal turbine blades[☆]

Amanda S.M. Smyth[a],[*], Federico Zilic de Arcos[a], Anna M. Young[b]

[a] *Department of Engineering Science, University of Oxford, Parks Road, Oxford, OX1 3PJ, UK*
[b] *Department of Mechanical Engineering, University of Bath, Claverton Down, BA2 7AY, Bath, UK*

ARTICLE INFO

Keywords:
Unsteady gust loading
3D effects
Theodorsen
Tidal power
Hydrodynamic modelling

ABSTRACT

This study investigates the blade loads on a model tidal turbine subject to unsteady gust forcing in the form of uniform small-amplitude oscillations in the axial inflow velocity. The validity of industry-standard 2D strip-theory models for calculating unsteady hydrodynamic loading on 3D rotor geometries is evaluated by comparing the 2D results to 3D simulations, both Reynolds-Averaged Navier Stokes (RANS) simulations and 3D inviscid vortex lattice modelling (VLM). The results show that the 2D function captures neither the trends nor the magnitudes of the unsteady turbine loads, which exceed the quasi-steady loads. The inviscid VLM corresponds more closely to unsteady RANS simulations, suggesting that 3D wake effects are a primary driver of the unsteady loads. A key non-dimensional parameter determining the unsteady load magnitudes is identified as the ratio of gust frequency to blade passing frequency. Finally, it is demonstrated that applying conventional tip-loss corrections to 2D unsteady hydrodynamic load models can in some circumstances lead to severely under-predicted blade loads. These outcomes have implications for the evaluation of peak and lifetime loads on tidal devices, and for any rotor application which relies on 2D strip-theory methods for unsteady load evaluation.

1. Introduction

In operation, tidal turbines are subjected to a range of unsteady and dynamic flow conditions, including surface waves, freestream turbulence, nonuniform inflow velocity, vortex shedding from upstream obstacles, and platform movement (Adcock et al., 2021). Surface waves have been identified as one of the largest source of unsteady loads on turbines (Scarlett et al., 2019). Tidal turbines experience larger loads than wind turbines of equivalent power (Winter, 2011; Adcock et al., 2021), meaning that even small perturbations in the inflow due to turbulence or waves can generate large loads that must be accounted for to accurately predict peak loads or fatigue damage (Mullings et al., 2017; Mullings and Stallard, 2021). Underestimation of blade loads prior to deployment is historically the most common cause of early turbine failure according to Walker and Thies (2021) (although it should be noted that as of the time of their study only four demonstration devices had failed in this way, which corresponded to 6% of the total number of deployed horizontal-axis tidal turbines). Consequently, the industry is working to resolve the problem of overloading (e.g. Slama et al., 2021; Fagan et al., 2019; McCarthy et al., 2022; Mullings and Stallard, 2021) to ensure long-term device reliability, which is

---

[☆] The computational work presented in this paper was carried out using resources provided by the Cambridge Tier-2 system operated by the University of Cambridge Research Computing Service (http://www.hpc.cam.ac.uk) funded by EPSRC Tier-2 capital grant EP/P020259/1. This project received funding from the European Union's Horizon 2020 research and innovation programme under the Marie Skłodowska-Curie grant agreement No 101034329, recipient of the WINNINGNormandy Program supported by the Normandy Region.

[*] Corresponding author.
E-mail address: amanda.smyth@eng.ox.ac.uk (A.S.M. Smyth).

https://doi.org/10.1016/j.jfluidstructs.2025.104381
Received 3 August 2024; Received in revised form 3 July 2025; Accepted 5 July 2025

one of the primary goals of tidal developers as they develop commercially viable devices (Walker and Thies, 2021). As such, it is necessary to have reliable predictions of unsteady hydrodynamic loading during the design process.

Industrial tidal turbine modelling relies on Blade Element Momentum (BEM) methods, which assume locally 2D flow with tip-loss corrections applied. If unsteady flow effects are considered, the Beddoes-Leishman dynamic stall model for 2D flow-aerofoil interaction (Leishman and Beddoes, 1989; Beddoes, 1993) is commonly implemented at the blade-element level (e.g. Scarlett et al., 2019), which simplifies to the classic 2D Theodorsen function (Theodorsen, 1935) in non-separated flow. The degree of unsteadiness in unsteady fluid-aerofoil interaction is quantified by the reduced frequency $k = \omega c/2U$ (Eq. (1) below), where the criterion for unsteadiness is considered to be $k > 0.05$.

Whether it is appropriate to assume locally 2D flow has been called into question given the low aspect ratios of tidal turbine blades and the significant spanwise flows than can develop (Winter, 2011; Wimshurst and Willden, 2018). Furthermore, studies of dynamic stall on finite-span wings reveal complex nonlinear features that differ significantly from 2D flow predictions (e.g. Visbal et al., 2013). Smyth et al. (2021) carried out a parametric study of the effects of 3D geometry features on unsteady small-amplitude gust response and found that the 3D response deviated significantly from 2D predictions. They identified the cause as the influence of three-dimensional wake vorticity: 2D models assume that vorticity shed from the trailing edge consist only of a spanwise component. However, for a 3D wing or rotor there is also a streamwise component of wake vorticity (most visible as the ‘tip vortex’ for finite wings and rotors). In steady flow the impact of streamwise tip vortices on rotors can be accounted for by tip-loss corrections (e.g., the commonly used Prandtl, 1921 correction), however Smyth et al. (2021) demonstrated that the influence of streamwise wake vorticity diminishes substantially for rotors in unsteady flow conditions, such that the 3D loads gradually approach the 2D load predictions with increasing reduced frequency. This suggests that steady tip-loss corrections such as the Prandtl model may be inappropriate for dynamic load evaluation, and that 2D-based methods such as BEM that rely on such corrections may not capture the full 3D unsteady flow physics.

Based on the above concerns about the suitability of the assumption of locally 2D flow for tidal turbine modelling, the aims of this study are: (1) to evaluate the extent of 3D effects in the load response of representative tidal turbine blades to unsteady inflow, (2) to identify relevant nondimensional groups that govern the unsteady turbine load response, and (3) to explore the implications for turbine modelling. These aims are achieved through a numerical parametric study using unsteady Reynolds-Averaged Navier Stokes (URANS) simulations, an inviscid 3D vortex lattice model (VLM), and the 2D Theodorsen function. A small-amplitude harmonic oscillation is applied to the axial inflow velocity. This idealised 1D gust is not representative of all gusts seen by operating turbines, but is similar to the inflow conditions that would be seen when operating in long-period surface waves (Sequeira and Miller, 2014). Furthermore, this idealised uniform gust represents the conditions for which the 2D Theodorsen function was developed, meaning that deviations from the 2D prediction of gust response can be attributed to the 3D geometry.

The paper is outlined as follows: Section 2 gives further details of relevant past studies, the computational modelling methods used, and the theory of unsteady fluid dynamics including analysis of relevant nondimensional groups in Section 2.3. Section 3 outlines the implementation of the numerical methods used in this paper, while Section 4 presents the results and discusses the implications for unsteady hydrodynamic modelling of tidal turbines. Finally, Section 5 discusses the implications for realistic flows seen by deployed tidal turbines.

2. Background

2.1. Dynamic loading in tidal turbines

There is significant uncertainty in existing prediction methods for unsteady turbine loads. For example, Holst et al. (2015) carried out URANS and BEM simulations of a model turbine operating in surface waves and found that the two methods had similar levels of accuracy compared to experiments, though neither fully captured the unsteady load response seen in the experiments. For example, the wave-induced thrust amplitudes predicted by URANS and BEM were both over 25%–70% lower than the experimental values. However, one reason for the discrepancy was likely the difficulty in fully replicating the experimental unsteady flow conditions in the numerical simulations. Galloway et al. (2014) modified a BEM model to include dynamic inflow and gravitational loads, and demonstrated improved agreement with experiments for the loads on a tidal turbine in waves and yawed flow. However, agreement in the out-of-plane bending moment was variable and the unsteady bending moment amplitude was often underpredicted by 30%–40%. Guo et al. (2018) showed good agreement between experiments and BEM for a turbine in waves, however the very low reduced frequencies used (<0.044) suggest that their cases were quasi-steady, meaning that the study did not fully evaluate the unsteady load prediction capability of the BEM code.

In the above studies a significant source of uncertainty is the degree to which the incoming flow is accurately represented in the BEM or CFD simulations. This issue has also been highlighted as a particular challenge when evaluating the predictive capability of BEM codes for wind turbines (Schepers et al., 2002). One way to reduce uncertainty in the unsteady inflow is to use prescribed turbine motion. Milne et al. (2013) carried out extensive experimental studies of forced oscillation on a model marine turbine, while Whelan et al. (2009) and McNae (2013) carried out experimental studies of various unsteady flow effects on a model turbine in a high-blockage flow. A phase lead was observed in the turbine loads relative to the forced motion, as well as a load increase relative to the quasi-steady values, which was attributed to the dynamic inflow induced by the unsteady wake. Milne (2014) compared their experimental results of a turbine in forced oscillatory motion to a 2D dynamic inflow model, and found it to over-predict the unsteady load amplitude; including a tip-loss correction, however, led to under-predicted unsteady loads. Whelan et al. (2009) validated an unsteady BEM code against experimental measurements of a highly blocked turbine in oscillatory motion and found good agreement, but the study does not give the reduced frequency of the motion, so the ability of the BEM to predict unsteady loads cannot be evaluated.

The studies cited above highlight the significant uncertainty in the accuracy of 2D strip-theory methods such as BEM for predicting unsteady loads on tidal turbines. The purpose of the present study is to investigate the shortcomings of 2D-based methods from a fluid physics perspective, in order to evaluate the applicability and limitations of BEM in unsteady flow and to suggest alternative, more accurate, methods for use beyond the limitations of BEM.

While studies of dynamic loading in tidal turbines are more limited, there are extensive studies on those occurring in helicopter rotors and wind turbines. The tools used to analyse dynamic loading in tidal turbines have been adapted from those used in wind turbine and helicopter modelling. However, there are key differences in design and operating conditions that make insights from wind turbine and helicopter studies less applicable to tidal turbines. Tidal turbines have significantly lower blade aspect ratios compared to both wind and helicopter rotors, thus calling into question the validity of 2D modelling approaches for tidal turbines (Winter, 2011). The small aspect ratios and relatively high thrust and torque loads encountered by tidal turbines means that many designers choose to make the blades rigid, such that hydroelastic effects are negligible in dynamic loading scenarios. This is in contrast to wind turbines which, due to the trend towards larger diameters and thus longer and more slender blades, are strongly impacted by aeroelastic effects characterised by fluid–structure coupling and nonlinear events such as dynamic stall (Wang et al., 2016; Jahani et al., 2022). As such, much recent work in dynamic loading of wind turbines focus on the coupled fluid–structure interaction problem (see e.g. Veers et al. (2023) for an overview). For tidal turbines, regular variations in inflow speeds due to e.g. shear layer interaction generally result in only small-amplitude variations in angle of attack around the design point (Sequeira and Miller, 2014). As such, while viscous stall phenomena such as dynamic stall have been observed (Scarlett et al., 2019; Scarlett and Viola, 2020), they appear to occur only in high waves, significant yaw, or when operating far from the design operating point. In this way tidal turbines differ from helicopter rotors, in that the latter are characterised by operational limit states caused by dynamic stall when in forward flight (Richez, 2018), and so the phenomenon of dynamic stall is crucial for exploring and expanding the regular-operation flight envelope. Much of recent research in dynamic loading for helicopters focus on large-amplitude gusts in the separated regime (Jones et al., 2022) and also commonly focuses on transient gust encounters rather than harmonic (e.g. Wild et al., 2024). By contrast, tidal turbines in regular operation are likely to operate in the pre-stall regime at or near their design point, except in extreme scenarios, and encounters mainly harmonic disturbances (Sequeira and Miller, 2014). As such, this paper does not focus on the dynamic stall phenomenon, but rather on evaluating the importance of 3D effects on dynamic loading in pre-stall conditions at the design point, which is more likely to be encountered by tidal turbines and is historically under-explored.

2.2. Dynamic load modelling

As described above, the most common method used for dynamic load modelling for tidal turbines is BEM, either quasi-steady (e.g. Apsley and Stansby, 2020) or in combination with 2D analytical models such as the Beddoes-Leishman dynamic stall model (e.g. Sequeira and Miller, 2014; Scarlett et al., 2019) which defaults to Theodorsen in pre-stall conditions. This can be considered a low-order engineering model, necessary in industrial design where low computational cost is required. However, it is also widely used in academic research.

Higher-order alternatives for computational modelling of dynamic loads on tidal turbines include (in approximate order of increasing computational cost) boundary element methods, actuator methods, URANS, DES and LES. Boundary element methods are based on solutions to the potential flow problem, which allows for superposition of discrete source, sink, doublet and vortex elements along the problem boundaries (e.g. on the blade and wake) to define the time-varying flow field in the whole 3D domain (Katz and Plotkin, 2001). Such Lagrangian methods can be solved substantially faster than field discretisation methods such as URANS and LES. However, since the potential flow problem is inherently inviscid, any viscous effects such as drag or far-wake development and dissipation must be accounted for through correction factors or other model extensions. Boundary element methods are widely used for the study of biological and bio-inspired swimming hydrodynamics (e.g. Moored, 2018; Ayancik et al., 2019), which is an inherently unsteady and three-dimensional flow problem. They are furthermore used in wind turbine modelling when considering dynamic wake effects in the near-wake region (e.g. Greco and Testa, 2021), and for modelling propellers and other turbomachinery (e.g. Turnock, 1993; Kinnas and Hsin, 2012). An advanced Lagrangian boundary element method intended for tidal turbine modelling was developed by Pinon et al. (2012) and has been used to study e.g. the effects of turbulence on wake development (Bex et al., 2020) and multi-turbine interaction (Dufour et al., 2024).

Common options for field-discretised high-order simulations for dynamic load modelling include URANS, DES and LES, either blade-resolved (e.g. Afgan et al., 2013; McNaughton et al., 2012; Wimshurst, 2018; Posa et al., 2024) or representing the blades as actuator surfaces (e.g. Shen et al., 2009) or momentum sources (e.g. Sørensen and Shen, 2002; Apsley et al., 2018; Schluntz and Willden, 2015). All of these options have substantially higher computational cost compared to BEM and boundary-element methods. Blade-resolved DES and LES has historically been unachievable for most practical tidal turbine simulations, with a few notable studies using this method including Afgan et al. (2013), Ahmed et al. (2017), Gu et al. (2020), Grondeau et al. (2020), Posa et al. (2021, 2024) and El Fajri et al. (2022). LES is considered the superior tool for studying turbine wake development due to the importance of turbulent interactions in the wake (Afgan et al., 2013; Posa et al., 2021), and actuator representations of the turbine (actuator discs, surfaces or lines) have been developed to reduce computational cost to enable multi-turbine interaction studies focusing on wake dynamics (e.g. Apsley et al., 2018; Ouro and Nishino, 2021). However, these actuator models ultimately rely on simplified model representations to obtain the turbine blade loads, usually through blade-element theory (Sørensen and Shen, 2002). As such, the associated blade loading calculations are subject to the same limitations and uncertainties as are associated with BEM, resulting from assuming locally 2D flow field on the blade (Wimshurst and Willden, 2017).

Because of the high computational costs required for high-fidelity blade-resolved LES and DES, it was not considered an option for the present parametric study of dynamic loading in tidal turbines. Furthermore, actuator disc or line representations of the blades in either LES or URANS was not considered due to the associated simplifications in the blade loading calculations. Blade-resolved URANS with wall functions has significantly lower computational cost compared to LES, and has demonstrated ability to accurately predict unsteady aerofoil response in pre-stall conditions (Lomele et al., 2025) while also capturing the blade-generated 3D flow features (e.g. tip and hub vortices, secondary vorticity) to sufficient accuracy in the near-wake region, if well-resolved and using appropriate turbulence closure models: Afgan et al. (2013) demonstrated that significant deviations between blade-resolved RANS and LES in the near-wake primarily occurred as a result of tip vortex interaction and breakdown due to proximity to the turbine support structure, while McNaughton et al. (2012) showed that $k-\omega$ SST closure (Menter et al., 2003) gave better predictions of turbine performance and near-wake characteristics compare to other closure models. El Fajri et al. (2022) also showed reasonable agreement between URANS and DES in the near-wake. Given that only the turbine blades are modelled in the present study, URANS with $k-\omega$ SST closure was deemed sufficient for capturing both dynamic loading and near-wake vortex structures.

The aim of the present study is to evaluate the limits of commonly-used 2D-based methods for calculating dynamic loads in low aspect ratio tidal turbine blades, through a comparative parametric study of a model turbine in simplified gust inflow conditions, using modelling methods at different fidelity levels. Based on the above options, the following three methods are used: blade-resolved URANS, a boundary-element inviscid vortex lattice model (VLM) developed in-house, and the 2D Theodorsen function. The latter two were used in a study by Smyth et al. (2021) to evaluate 3D geometry effects on gust-induced loads for simplified wing and rotor geometries. In their study, a key difference between the 2D function and 3D VLM was identified as streamwise vorticity effects (which includes the tip vortex), which are not included in the 2D model. For a 2D geometry the VLM and Theodorsen function give identical results, but for finite aspect ratios the 3D VLM can differ substantially due to the presence of streamwise vorticity. As such, by comparing the 2D Theodorsen predictions to those of 3D inviscid VLM in the present study, we evaluate the importance of aspect ratio effects and streamwise wake vorticity in the dynamic loading of tidal turbines. Note however that the VLM is fully inviscid, meaning that it cannot capture phenomena such as viscous drag or stall, and that VLM does not explicitly consider spanwise flow effects but rather adjusts the velocity inflow angle to account for wake downwash. As such, by further comparing the Theodorsen and VLM results to blade-resolved URANS we evaluate the relative importance of viscous effects and spanwise flows for small-amplitude gusts.

2.3. Classical aerofoil theory and returning wake effects

This section introduces the analytical 2D Theodorsen and Loewy functions in more detail, and they are then used to identify relevant nondimensional groups for characterising the dynamic load response of tidal turbines. The functions both assume 2D inviscid (potential) flow with small-amplitude harmonic perturbations. They are parameterised by the reduced frequency:

$$k = \frac{\omega c}{2U} = \frac{\omega b}{U} \tag{1}$$

where ω is the forcing frequency in rad/s, U is the local relative inflow velocity, c is the chord and b is the semi-chord.

The Theodorsen function is denoted $C(k)$, and the unsteady lift at time t resulting from a gust acting uniformly along the aerofoil chord is given by the real component of the following function:

$$C_L = [2\pi C(k) + i\pi k]\,\hat{\alpha} e^{i\omega t} \tag{2}$$

Here $\hat{\alpha}$ is the amplitude of the angle of attack oscillations. The Theodorsen function is given by:

$$C(k) = \frac{H_1^{(2)}(k)}{H_1^{(2)}(k) + iH_0^{(2)}(k)} \tag{3}$$

where $H_v^{(2)}$ is a Hankel function of the second kind, of order v.

Unsteady lift is governed by the induced flow on the foil from the vorticity shed from the trailing edge with the changing angle of attack. For rotor blades, the wake has a helical shape, resulting in a 'returning wake' (see Fig. 1a). Loewy (1957) developed an extension to the Theodorsen function, intended for helicopter rotor modelling, that accounted for returning wake effects. Sequeira and Miller (2014) found it necessary to use the Loewy function rather than the Theodorsen function to accurately capture wave-induced loads on 2D tidal turbine aerofoils. Fig. 1b illustrates the model for returning wake effects in the 2D rotating reference frame. The impact of the returning wake on the aerofoil loading is determined by (1) the proximity of the returning wake segments (h in Fig. 1b), and (2) the phase of the returning wake vortex strength relative to the aerofoil location (Ψ in Fig. 1b). The Loewy function $C'(k, \frac{\omega}{N_b\Omega}, \frac{h}{b}, \Delta\Psi, \frac{\omega}{\Omega})$ modulates the Theodorsen function through a parameter W, giving the degree of returning wake interference:

$$C'(k, \frac{\omega}{N_b\Omega}, \frac{h}{b}, \Delta\Psi, \frac{\omega}{\Omega}) = \frac{H_1^{(2)}(k) + 2J_1(k)W}{H_1^{(2)}(k) + iH_0^{(2)}(k) + 2[J_1(k) + iJ_0(k)]W} \tag{4}$$

$$W(k, \frac{\omega}{N_b\Omega}, \frac{h}{b}, \Delta\Psi, \frac{\omega}{\Omega}) = 1/(e^{kh/b} e^{i2\pi(\omega/N_b\Omega)} e^{i\Delta\Psi\omega/\Omega} - 1) \tag{5}$$

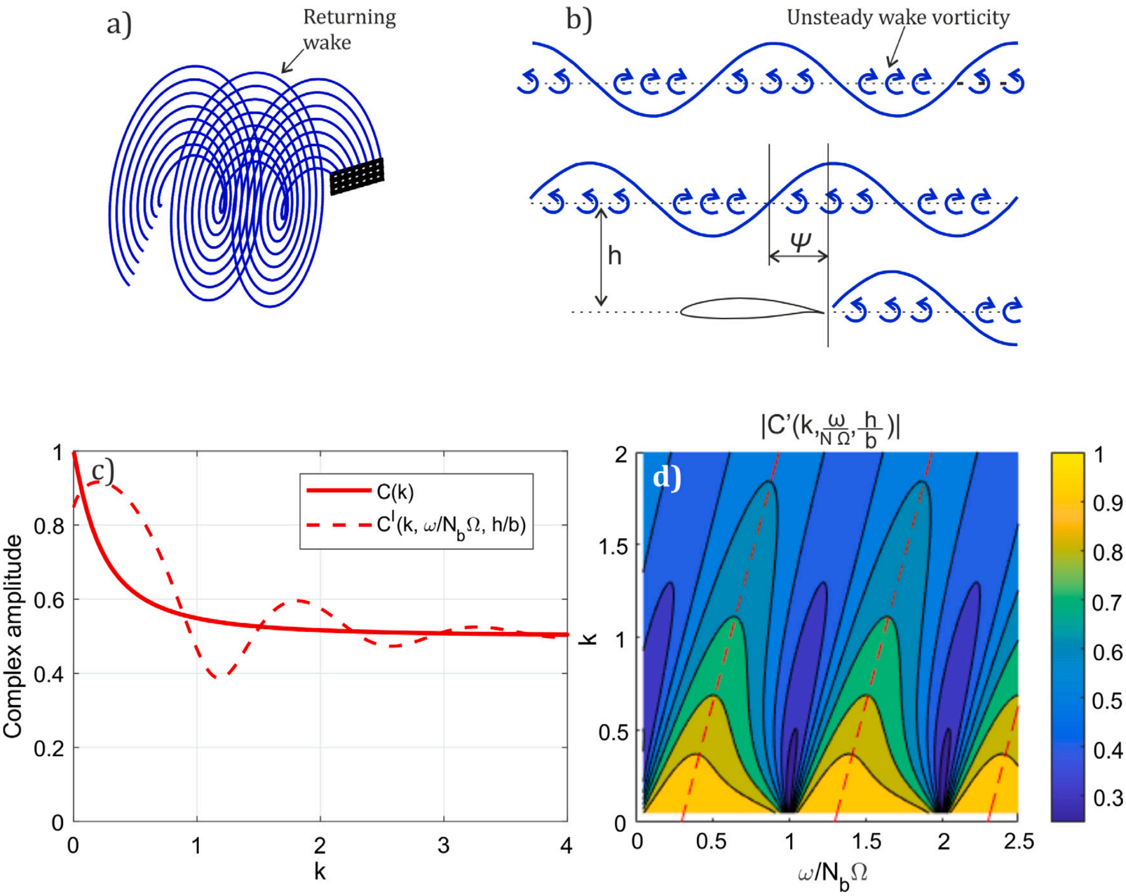

Fig. 1. (a) Simple illustration of a helical returning wake being shed from a rotor blade. (b) 2D section view of the returning wake. (c) Amplitude of the Theodorsen and Loewy functions against reduced frequency k, the Loewy function evaluated for $N_b = \Omega = h/b = 1$. (d) Contours show the complex amplitude of the Loewy function for $N_b = \Omega = h/b = 1$, against reduced frequency on the y-axis and frequency ratio on the x-axis.

Here N_b is the number of blades, Ω the blade rotational frequency in rad/s and $\Delta\Psi$ the wake phase change caused by swirl velocity. J_v is the Bessel function of the first kind, of order v. If the axial wake velocity is assumed equal to the freestream velocity U_∞ such that $h = 2\pi U_\infty / N_b\Omega$, and assuming swirl velocity to be negligible ($\Delta\Psi = 0$), we can simplify as follows:

$$W(k, \lambda, \sigma, \frac{\omega}{N_b\Omega}) = 1/(e^{(k/\sigma\lambda)} e^{i2\pi(\omega/N_b\Omega)} - 1) \tag{6}$$

where λ is the local tip-speed ratio $r\Omega/U_\infty$ and the blade solidity σ is given by $\sigma = N_b c/2\pi r$ where r is the local radius. If W is small, returning wake effects are negligible and the Loewy function is equal to the Theodorsen function.

The first exponential in Eq. (6) causes W to decrease with decreasing tip-speed ratio (TSR) and with increasing reduced frequency k. The second exponential is determined by a nondimensional parameter that we will call the ‘frequency ratio’:

$$\frac{\omega}{N_b\Omega} \tag{7}$$

This is the ratio between the gust frequency ω and the blade-passing frequency $N_b\Omega$. A typical effect of the returning wake is illustrated in Fig. 1c, which shows the amplitude of the Theodorsen function $C(k)$ compared to that of the Loewy function $C'(k, \omega/N_b\Omega, h/b)$ over a range of reduced frequencies, for $h/b = N_b = \Omega = 1$. The amplitude of the Loewy function can be seen to oscillate around the Theodorsen function with increasing k, as the returning wake alternates between amplifying and attenuating the unsteady response.

The forcing frequencies at which the peaks of the Loewy function occur are a function of the three nondimensional variables k, $\omega/N_b\Omega$ and h/b. However, the strongest predictor is the frequency ratio $\omega/N_b\Omega$. This is illustrated in Fig. 1d, which shows the magnitude of the Loewy function as contours against the frequency ratio on the x-axis and the reduced frequency on the y-axis, again for $h/b = N_b = \Omega = 1$. Unlike in Fig. 1c, the local chord length and/or the axial inflow velocity is changed in order to vary the reduced frequency k at a given fixed frequency ratio in Fig. 1d. It can be seen that the Loewy function peaks diminish with increasing k, and that the peaks occur at regular intervals determined by the frequency ratio. However, the peaks shift such that they occur at higher frequency ratios as the reduced frequency increases. The dashed red lines in Fig. 1d indicate an approximation for the location of the peaks given by:

$$(\omega/N_b\Omega)_{peak} = k/\pi + \Delta\Phi + n \tag{8}$$

where the phase $\Delta\Phi$ is taken as 0.3, and n is 0 or an integer. The phase $\Delta\Phi$ is a weak function of h/b: for $h/b = 0.1$, $\Delta\Phi$ was found to be approximately 0.25, while for $h/b = 32$, $\Delta\Phi$ was found to be approximately 0.45. As a result, the value of $\Delta\Phi = 0.3$ as used in Fig. 1d can be considered a good approximation within the range of realistic h/b values (h/b for a 3-bladed turbine with solidity 0.1 would be approximately 2.5 at TSR 4). Thus the ratio h/b, which is set by the TSR, can be said to primarily determine the amplitude of the Loewy function, while the forcing frequency at which the peak value occurs is determined by the frequency ratio and the reduced frequency, with the frequency ratio having the largest impact. Based on the analysis of Sequeira and Miller (2014), tidal turbines are expected to experience unsteady flow in the range $k = 0 - 0.7$, resulting in a likely range for $(\omega/N_b\Omega)_{peak}$ of approximately $0.3 - 0.52$ for $n = 0$. The model turbine used in this study will be shown below to have a peak load amplitude at approximately $\omega/N_b\Omega = 0.4$. It should be noted that the overall maximum harmonic load amplitude may or may not occur at $(\omega/N_b\Omega)_{peak}$: depending on flow and geometry configurations, the peak load amplitude could occur at quasi-steady frequencies ($\omega/N_b\Omega \approx 0$). However, for low-aspect ratio blades with noticeable returning wake effects, such as the blades analysed in this paper, the peak load likely occurs at $(\omega/N_b\Omega)_{peak}$.

The analysis in this section, and the results presented below in Section 4, show that the frequency ratio is a primary indicator for the magnitude of harmonic gust loading on a tidal turbine. It should be noted that while it is arguably most appropriate to compare the 3D simulation results in this paper to the 2D Loewy function, in the remainder of this paper we compare results only to the Theodorsen function. This is because the Theodorsen function is more commonly used in BEM codes for tidal turbines (Sequeira and Miller, 2014; Scarlett et al., 2019), and also because for the turbine blades used in this paper the differences between Loewy and Theodorsen load predictions were small (Smyth et al., 2019). Only at nearly quasi-steady frequencies was there a clear difference between the two functions. However, it will be shown below that despite the weak influence of the returning wake predicted by the 2D function, in the results from the 3D simulations in Section 4.2.3 the frequency ratio is a significant indicator of the overall load magnitude. But first the different numerical modelling methods used in this study and the simulation setup will be introduced in more detail in Section 3 below.

3. Simulation methodology

3.1. The vortex lattice model

The VLM used in this paper is a frequency-domain model assuming small-amplitude perturbations, equivalent to that used by Smyth et al. (2021). Given matching flow assumptions (small-amplitude 2D potential flow), the VLM gives results identical to classical unsteady aerofoil theory, e.g. the Theodorsen function. The model is based on that outlined by Katz and Plotkin (2001) with modifications to allow for frequency-domain modelling.

In VLM the bound vorticity of the blade is represented by vortex rings, which are shed from the trailing edge into the freestream at each time step to form the wake. The forces and boundary conditions are evaluated on the collocation point on each panel. The Kutta condition is implicitly enforced by placing the collocation points at 3/4 length of each panel and the spanwise bound vorticity vector at 1/4 length. A general illustration of the VLM format can be seen in Fig. 2a, and the specific application to the turbine geometry of the present study is shown in Fig. 2b. Note that only the blades are modelled in the VLM, not the turbine hub or support structure.

Applying the boundary condition of zero surface-normal flow results in a system of simultaneous equations of the form:

$$\mathbf{A}\boldsymbol{\Gamma} + \mathbf{u} = 0 \tag{9}$$

where $\boldsymbol{\Gamma}$ is the bound circulation, $\mathbf{u}$ is the surface-normal velocity vector, and $\mathbf{A}$ is the transform matrix applying the Biot–Savart law, which gives induced velocity by the wake and panel vortices at each collocation point. The circulation of each wake vortex ring is equal to the strength of the trailing-edge panel vortex at the time it was shed into the wake. The VLM thus allows for the direct inclusion of unsteady wake vorticity effects caused by time-varying inflow velocity, which in BEM must be estimated from the Theodorsen function (see Section 2.3). The 3D VLM format allows for adjacent blade and wake interaction through the vortex-induced downwash, as opposed to BEM which assumes each 2D blade section to be unaffected by the others.

Having obtained the bound circulation vector $\boldsymbol{\Gamma}$ by inverting $\mathbf{A}$ in Eq. (9), the resulting local force vector is calculated from the vector form of the Kutta-Joukowski theorem:

$$\mathbf{F} = \rho(\mathbf{u} \times \boldsymbol{\Gamma}) + \rho\Delta S\frac{\partial|\boldsymbol{\Gamma}|}{\partial t} \tag{10}$$

The first component on the right hand side of Eq. (10) represents the circulatory forces, while the second – the time-derivative of the bound circulation – gives the added mass force. ΔS is the surface area of the lattice cell. The lattice resolution used to obtain the results in this paper was 20 chordwise and 20 spanwise panels, resulting in 1200 collocation points for the three blades. The VLM version used in this paper has been validated for modelling wing and rotor geometries, and mesh resolution studies were carried out before choosing the above lattice resolution; more details of the implementation and validation can be found in Smyth et al. (2021) and Smyth (2020).

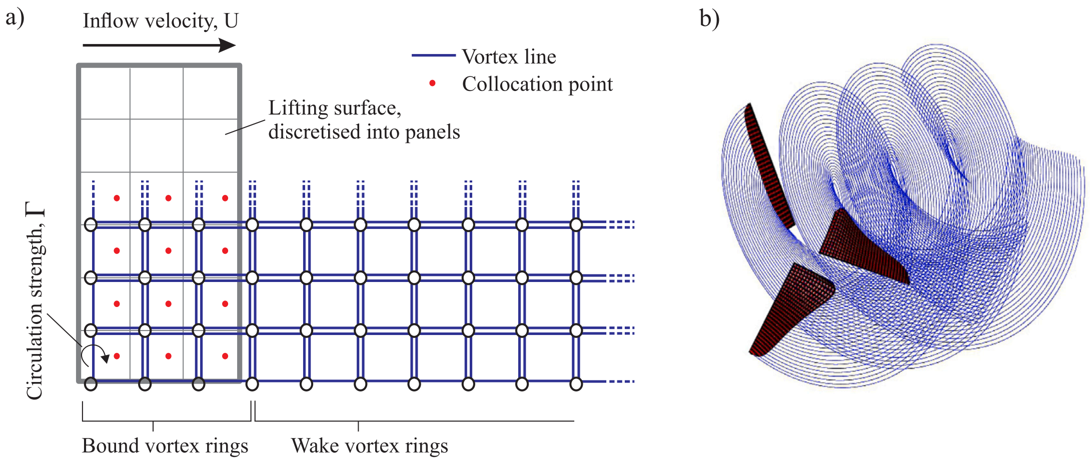

Fig. 2. (a) Illustration of the structure of the VLM, in the case of a rectangular wing. (b) Illustration of the model tidal turbine as represented in VLM, with a prescribed wake.

Drag, stall and other viscous effects are not included in this inviscid model, and neither is the effect of aerofoil thickness. A prescribed wake is used, but in order to obtain an estimate of the effects of vortex rollup on the unsteady loading, two prescribed wake configurations have been implemented: In the first model, wake vortices are assumed to move downstream at the freestream velocity U_∞, with no further deformation. In the second model (denoted VLM-w), the wake is allowed to develop in steady flow in a time-stepping version of the VLM, which includes wake vortex self-interaction. The resulting wake topology is then used in the unsteady frequency-domain calculations, effectively assuming that the unsteady flow has negligible effect on the wake shape. A more detailed study of the impact of different prescribed wake topologies was carried out by Smyth and Young (2019) and by Smyth (2020).

3.2. RANS modelling

Steady and unsteady RANS modelling was carried out using the open-source CFD software OpenFOAM, using the 'SRFSimpleFoam' and the 'pimpleDyMFoam' solvers. The turbulence model used was $k-\omega$ SST (Menter et al., 2003), which has been employed extensively in tidal turbine modelling (McNaughton et al., 2012; Afgan et al., 2013; Sequeira and Miller, 2014). The computational domain size is illustrated in Fig. 3a; on doubling the exit or entry domain lengths the steady-state turbine performance changed by less than 1%, ensuring domain size convergence. The radial distance was chosen to achieve a comparable blockage (about 12%) to experimental tests of this model turbine, carried out at Ifremer in Boulogne-sur-Mer, France (Young et al., 2016). A third of the turbine annulus was modelled, with periodic boundaries (see Fig. 3b). The turbine hub, nacelle and support structure were not included, as this study focuses only on the unsteady flow interaction with the turbine blades. The central and farfield domain boundaries were set to slip walls, and the radius of the central domain boundary was equal to the turbine hub radius (0.0555 m).

The surface mesh of the blade is shown in Fig. 3b. The target $y+$ value was 60, and wall functions were used to represent boundary layer effects. The pressure and suction surfaces each have 110 cells, while the rounded trailing edge has 12 cells. A spanwise cell count of 79 was used, with cells clustered towards the hub and tip. Doubling the spanwise cell count had negligible effect on the steady-state turbine performance. The total cell count was approximately 17 million, for the simulated domain of one-third of the turbine annulus. The required chordwise aerofoil resolution and $y+$ value were determined through preliminary 2D mesh convergence tests of the NACA 63421 blade section (Smyth, 2020). The sectional 2D lift curve is shown in Fig. 3c, as obtained by RANS simulations at Reynolds number (Re) of 7.6×10^5 and in experimental measurements at $Re = 1.41 - 2.08 \times 10^5$ (Young and Smyth, 2021). The RANS results can be seen to agree with experiments until the aerofoil stall angle at angle of attack approximately 9°, after which the experimental results have a lower value of lift. This deviation between RANS and experimental results is likely due to the gradual trailing-edge stall which is characteristic of this aerofoil, which may be difficult to capture by the RANS with wall functions used in this study. As such, post-stall RANS and URANS results may not be as reliable as pre-stall results. Since the present study focuses on small-amplitude flow perturbations, this should not significantly affect the results: Fig. 3d shows the spanwise angle of attack distributions for TSR 3.25 and 5, obtained using the line-average flow sampling method (Jost et al., 2018) on the steady RANS simulations. The measured angle of attack range can be seen to be within the linear lift regime of Fig. 3c, except for close to the hub and tip where the flow sampling method is less reliable (Zilic de Arcos et al., 2020). Given that the maximum unsteady inflow amplitude used in this study is 15% of the mean inflow speed (see Section 3.4), translating to a maximum unsteady TSR range of 3.48–4.7, Fig. 3c and d suggest that the unsteady response should be in the linear regime along most of the span for the cases shown in this paper.

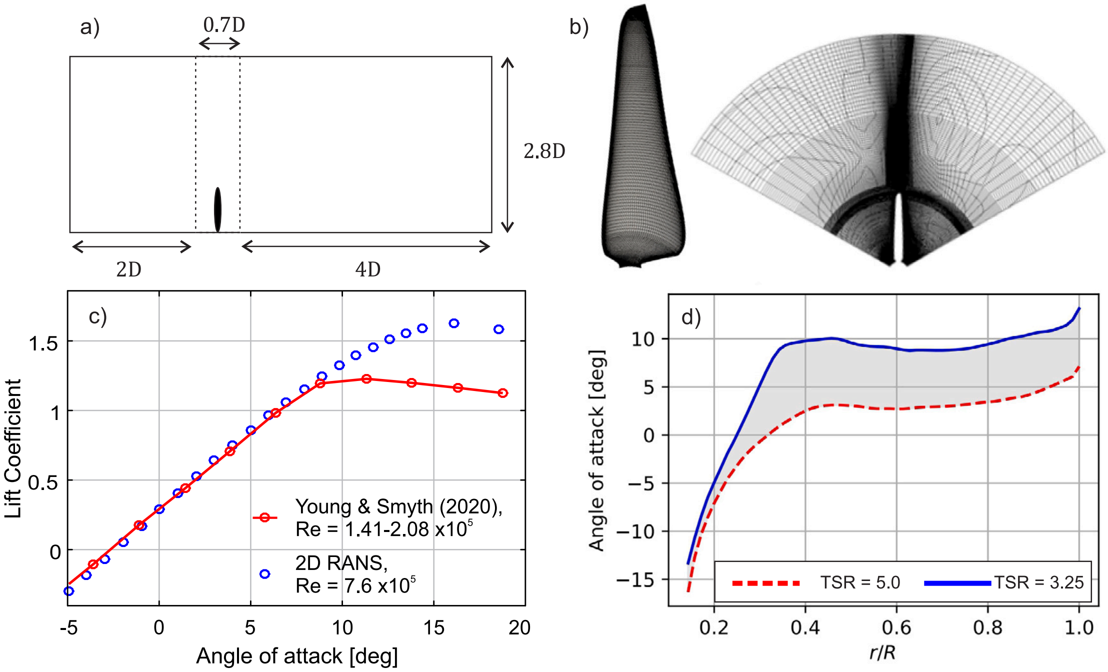

Fig. 3. (a) Size of the 3D RANS/URANS computational domain. (b) Blade surface and axial cross-section of the mesh used for 3D RANS/URANS simulations. (c) Aerofoil lift curve for the NACA 63421 blade section used, obtained from preliminary 2D RANS simulations. (d) Spanwise distributions of angle of attack obtained from the steady 3D RANS simulations.

All results shown below are obtained from data recorded after the unsteady turbine wake had reached the domain exit, as this was found to be necessary for load convergence. In order to speed up this startup stage of the simulations, the time step of the URANS simulations was constrained such that the Courant number was <1000 while the unsteady wake was propagating through the domain. It was then reduced to <100 for at least one full load cycle when the unsteady wake had reached the domain exit, and then finally to <10 for up one further load cycle to ensure that the results did not change further with the reduced time step. While it is normally necessary to ensure Courant number <1 for numerical stability, the PIMPLE algorithm available in OpenFOAM allows for larger Courant numbers by iterating the solution and applying under-relaxation between time steps. Consequently the solution remains stable, but unsteady flow field information occurring over shorter time scales is lost. As such, the larger Courant number used during the startup sequence resulted in effectively lower numerical time-step resolution, however this was considered acceptable during the startup sequence as macro-scale properties of the unsteady wake were still captured. A Courant number of 100, used subsequently to record the blade loads, results in a time step that can capture frequencies up to 1700 Hz according to the Nyquist criterion, and corresponds to about 0.2 degrees of turbine rotation per time step. The turbine rotational frequency was 1.82 Hz (109 rpm) and the highest gust frequency tested was 6.25 Hz. Further details of the simulations and the mesh resolution studies can be found in Smyth (2020).

3.3. 2D dynamic load modelling using the Theodorsen function

The industry-standard modelling tool for dynamic loading in tidal turbines is BEM, either assuming quasi-steady conditions (e.g. Apsley and Stansby, 2020) or using the semi-analytical Beddoes-Leishman function for 2D aerofoil dynamic stall (e.g. Moriarty and Hansen, 2005; Galloway et al., 2014; Scarlett et al., 2019), which defaults to the Theodorsen function in pre-stall conditions. To compare the VLM and URANS dynamic load simulations in this paper to what might be predicted by a BEM code, we evaluate the Theodorsen function (Eq. (2)) along the blade span and integrate to find the total blade dynamic loads.

The Theodorsen function is evaluated over the same number of spanwise blade sections as there are spanwise lattice panels in the VLM, that is 20 evenly spaced spanwise locations. At each position the local chord length, relative inflow velocity and gust frequency are used to find the local reduced frequency (Eq. (1)). The resulting unsteady lift for a given angle of attack amplitude $\hat{\alpha}$ is then evaluated using Eq. (2).

To evaluate the local relative inflow velocity U and the angle of attack amplitude $\hat{\alpha}$ induced by the gust, we consider the axial induction factor to be negligible. The relative inflow velocity at radial position r is then found from the inflow velocity and turbine rotational speed as:

$$U(r) = \sqrt{U_\infty^2 + (\Omega r)^2} \tag{11}$$

Table 1

Approximate local Reynolds numbers, reduced frequencies and gust amplitudes at different radial positions. The mean relative inflow velocity U is calculated from the undisturbed farfield velocity U_∞ and the local blade speed, with no induction factors applied. The reduced frequency range corresponds to the oscillation frequencies ω used in the URANS simulations in this study.

Radial position r/R	Reynolds number $Re = cU/\upsilon$	Reduced frequency $k = \omega b/U$	Reduced frequency, URANS range	Gust amplitude $\hat{\alpha}$ for $\epsilon = 0.15$
0.25	~118,000	0.039ω	0.24–1.58	4.3°
0.5	~132,000	0.018ω	0.11–0.71	3.4°
0.75	~126,000	0.008ω	0.05–0.33	2.6°

where U_∞ is the mean axial inflow speed. The angle of attack amplitude is then found as:

$$\hat{\alpha}(r) = \tan^{-1}\left(\frac{U_\infty + \hat{u}}{\Omega r}\right) - \tan^{-1}\left(\frac{U_\infty}{\Omega r}\right) \tag{12}$$

where $\hat{u}$ is the gust amplitude, in this study either 15% or 7.5% of the mean axial flow speed.

BEM is generally used with tip-loss corrections such as the Prandtl (1921) model to account for load reduction near the turbine hub and tip. While we do not apply any tip-loss corrections to the 2D dynamic results in Section 4.2 (for reasons that will be discussed below), in Section 4.3 we evaluate the effects of applying a simple tip-loss correction to the Theodorsen function predictions: the lift amplitude at each spanwise section is normalised by a constant value such that at $k \approx 0$ the amplitude is equal to that of the VLM. This effectively represents a numerical tip-loss correction based on the quasi-steady VLM results. While this does not fully represent how tip effects are modelled in BEM, it illustrates the potential negative consequences of applying a quasi-steady tip-loss correction to 2D unsteady aerofoil theory results.

3.4. *Gust properties and turbine geometry parameters*

The mean flow speed of all simulated cases is $U_\infty = 1$ ms^{-1}, and the turbine is rotated at the design TSR of 4, leading to a Reynolds number in the order 132,000 at mid-span of the model turbine based on the local chord length of 75 mm (see Table 1). Flow oscillation at frequency ω is added to the mean flow, such that the axial inflow velocity at a given time t is:

$$u = U_\infty[1 + \epsilon \sin(\omega t)] \tag{13}$$

where ϵ is the unsteady flow amplitude as a fraction of the mean flow speed. In the present study the majority of cases have $\epsilon = 0.15$, which as mentioned above translates to an effective TSR range of 3.48–4.7. This results in approximately 3.4° amplitude in the relative harmonic inflow angle at mid-span, although near the blade tip the amplitude will be lower and near the root it will be higher. The gust amplitude is calculated based on the farfield velocity and turbine rotational speed, not accounting for induction factors (see Eq. (12)). A small number of turbine simulations were repeated at $\epsilon = 0.075$, and the unsteady torque and thrust amplitudes normalised by ϵ changed by less than 5% as a result. This suggests the results presented below are invariant with amplitude, meaning that stall and related nonlinear effects are small for the analysed cases. In the simulations the turbine operates at constant rotational speed at its design TSR of 4 based on the mean flow velocity U_∞, so does not change with the unsteady inflow.

The turbine blades simulated in this study are those of an existing 0.7 m diameter model turbine which has been used extensively in past experimental studies (Young et al., 2016). Blade chord and twist distributions are shown in Fig. 4a. The blade aspect ratio AR is 4.2, defined as:

$$AR = \frac{(\Delta R)^2}{S_b} \tag{14}$$

where ΔR is the distance between the blade tip and hub, and S_b is the blade surface area. Further details of the turbine design and performance can be found in Smyth (2020) and Young et al. (2016).

Table 1 gives estimates of the Reynolds numbers Re, reduced frequencies, k, and relative inflow angle amplitudes $\hat{\alpha}$ at three spanwise locations along the turbine blade. Values are based on the local blade chord, c, the gust amplitude ϵ as defined in Eq. (13), and estimates of the local relative inflow velocity (Eq. (11)). Note that no induction factor was included in calculating U, meaning that the values for Re and the relative gust amplitude $\hat{\alpha}$ in Table 1 and the reduced frequency k may be slightly under-predicted. This choice was made because of the difficulty in measuring the local induction factor accurately, especially in harmonic unsteady flow, and so the values in Table 1 can be considered a first-order estimate.

The reduced frequency ranges given in the fourth column of Table 1 are based on the unsteady flow conditions simulated using URANS. The reduced frequencies increase with decreasing radial position, such that the turbine hub experiences strongly unsteady conditions while the flow near the blade tip can be considered quasi-steady for the lowest frequency cases. The hub also experiences the largest relative gust amplitudes, as can be seen in the final column of Table 1.

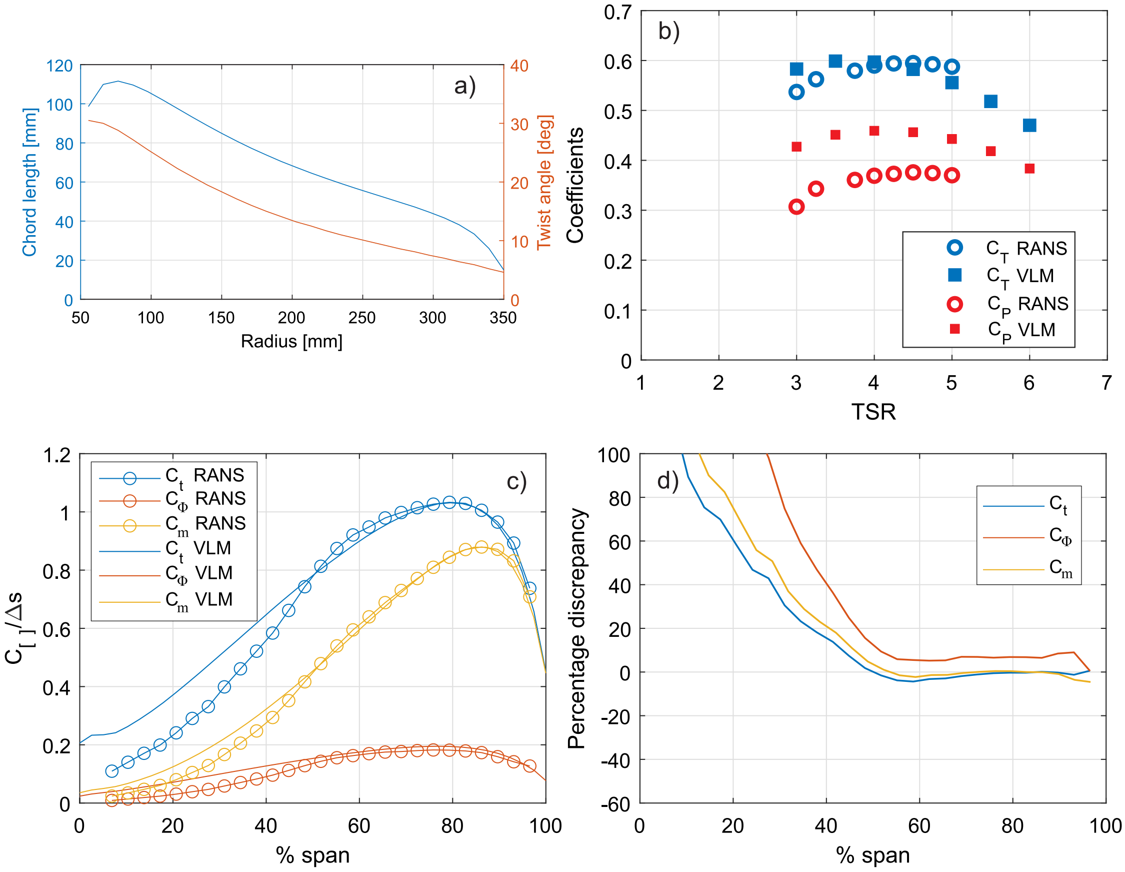

Fig. 4. (a) Blade chord and twist distributions. (b) Steady flow thrust and power coefficients. (c) Spanwise distribution of thrust, in-plane and out-of-plane moment coefficients per unit span for steady flow at TSR 4. (d) Discrepancy in the spanwise loads as predicted by VLM compared to RANS for steady flow at TSR 4. (For interpretation of the references to colour in this figure legend, the reader is referred to the web version of this article.)

4. Results

4.1. Steady flow

Fig. 4 shows the steady turbine performance from the RANS and VLM simulations. Fig. 4b shows the thrust and power coefficients against TSR, defined respectively as:

$$C_T = \frac{T}{\frac{1}{2}\rho U_\infty^2 S} \tag{15}$$

$$C_P = \frac{Q\Omega}{\frac{1}{2}\rho U_\infty^3 S} \tag{16}$$

where T and Q are the total thrust and torque and S is the turbine swept area. Looking first at the thrust (blue markers in Fig. 4b), the inviscid VLM and the RANS simulations show agreement to within 10% for the full TSR range, and closer for the design TSR of 4 where the VLM prediction is within 2% of the RANS. The peak thrust as predicted by VLM occurs at slightly lower TSR compared to the RANS simulations.

Looking at the power coefficient (orange markers in Fig. 4b), the magnitude is over-predicted by approximately 20% by the VLM compared to RANS at TSR 4. This is expected, as the turbine torque is more strongly affected by viscous drag than the thrust coefficient, and the VLM is inviscid. However, this discrepancy does not translate to the unsteady loading, as will be shown below in Section 4.2.

The power coefficient peaks at the design TSR of 4 in the VLM prediction, but at TSR 4.5 for the RANS, although the power coefficient does not vary strongly in the TSR range 4–5. This difference between RANS and VLM may be caused by the higher flow blockage in the RANS simulations (the RANS has about 12% blockage while the VLM has none). The biggest discrepancy between VLM and URANS occurs at TSR 3 in Fig. 4b. This is expected, as the blade gradually stalls with decreasing TSR; a process which is not captured by the inviscid VLM. In the remainder of this paper, all results are obtained at the design TSR of 4.

Fig. 4c shows the spanwise distribution of the axial (thrust) force coefficient and the in-plane (torque) and out-of-plane (flapwise) moment coefficients per unit span, respectively defined as:

$$C_t = \frac{f_x}{\frac{1}{2}\rho U_\infty^2 S} \tag{17}$$

$$C_\Phi = \frac{m_x}{\frac{1}{2}\rho U_\infty^2 S R} \tag{18}$$

$$C_m = \frac{m_f}{\frac{1}{2}\rho U_\infty S R} \tag{19}$$

where f_x, m_x and m_f respectively are the thrust force, the in-plane torque and the out-of-plane (flapwise) bending moment per unit span locally at a given spanwise location. R is the turbine radius. The spanwise load distributions show excellent agreement between RANS and VLM at the outer 50% of the blade span in Fig. 4c, with only a slight over-prediction of the tangential force by the inviscid solver. A more significant discrepancy is seen in the inner 50% of the blade span. This may be caused by the lower Re at the inboard blade sections, resulting in more significant effects of viscosity which is not captured by VLM. The viscous effects contribute to increased aerofoil drag, which primarily works to oppose the tangential force component while having a smaller effect on thrust. This may explain why the discrepancy at the inboard span sections is primarily visible in the tangential force. This can be seen more clearly in Fig. 4d, which shows the percentage discrepancy in the VLM predictions of the spanwise loads in steady flow, compared to the RANS results. The agreement over the outer half of the blade span is within 10% for both the thrust and moment coefficients. Below 50% span there is a gradually increasing discrepancy, with the in-plane moment coefficient seeing a more rapid increase: the local in-plane moment from VLM is double the RANS result by approximately 27% span, while the VLM thrust reaches double the RANS result by 10% span.

We can conclude from Fig. 4c and d that the over-prediction of the power coefficient by VLM, seen in Fig. 4b, is caused by over-prediction of in-plane bending moment in the innermost 50% of the blade span by the inviscid solver. While it is clear from Fig. 4d that the discrepancy between the inviscid VLM and the viscous RANS increases over the inner 50% of the turbine blade, it should be noted that the absolute blade forces also decrease substantially in this region (seen in Fig. 4c). As such, the discrepancy in the inviscid model is marginal for the total thrust coefficient in Fig. 4b, and it will be demonstrated below that the power coefficient is also predicted with good agreement by the inviscid solver in unsteady flow conditions.

4.2. *Unsteady flow performance*

4.2.1. *Flow field and wake*

Prior to quantitative analysis of the unsteady loading, a qualitative examination of the blade tip vortices gives insight into the potential causes for discrepancy between the viscous and inviscid simulations. Fig. 5 illustrates the helical wake tip vortices obtained from URANS simulations, visualised using the Q-criterion. Since the unsteady flow field is periodic around the annulus, the single-blade simulations have been repeated to create the full three-bladed domain for clarity. Dotted red lines mark the periodic domain side boundaries in Fig. 5. Fig. 5a shows the steady flow, while Fig. 5b shows an example of the tip vortex structure and other secondary vorticity features occurring in unsteady flow for frequency ratio $\omega/N_b\Omega = 0.65$.

Looking at the unsteady wake in Fig. 5b, there are some notable differences compared to the steady wake in Fig. 5a. The wake tip vortices are displaced relative to those in the steady case, indicating that tip vortex instabilities have developed. This effect would not be captured in the VLM, since it assumes a fixed wake shape. However, a previous study by the authors (Smyth and Young, 2019) suggests the impact of this wake displacement on the unsteady loading is small. For more details on the observed tip vortex instabilities, their relationship to the frequency ratio and their impact on the downstream wake development, see Smyth et al. (2023).

Another difference between steady and unsteady wakes in Fig. 5 is the increase in secondary vorticity shed along the span (indicated in Fig. 5a and b). While the steady-flow secondary vorticity has mostly dissipated when it reaches the periodic side boundary, the unsteady flow case still has secondary vorticity present at the periodic boundary. The periodic boundary condition then appears to cause dissipation of the remaining secondary vorticity. This should be recognised as a potential source of error for the present URANS simulations.

Looking at the hub region of the turbine in Fig. 5b, significant levels of shed vorticity can also be seen (indicated as ‘hub vorticity’ in Fig. 5b); these are not present in the steady flow case in Fig. 5a. This vortex shedding is likely caused by flow separation, due to the larger angle of attack amplitudes at the inboard blade sections (see Table 1). Fig. 5b includes a detail of the turbine in unsteady flow, showing large regions of vorticity around the trailing edge near the turbine hub, suggesting separated flow in this area. This is also a potential source of discrepancy between the VLM and URANS, as the VLM does not capture stall or other viscous effects. However, as will be shown below, the VLM is still capable of accurate first-order predictions of the integrated unsteady loads despite these discrepancies.

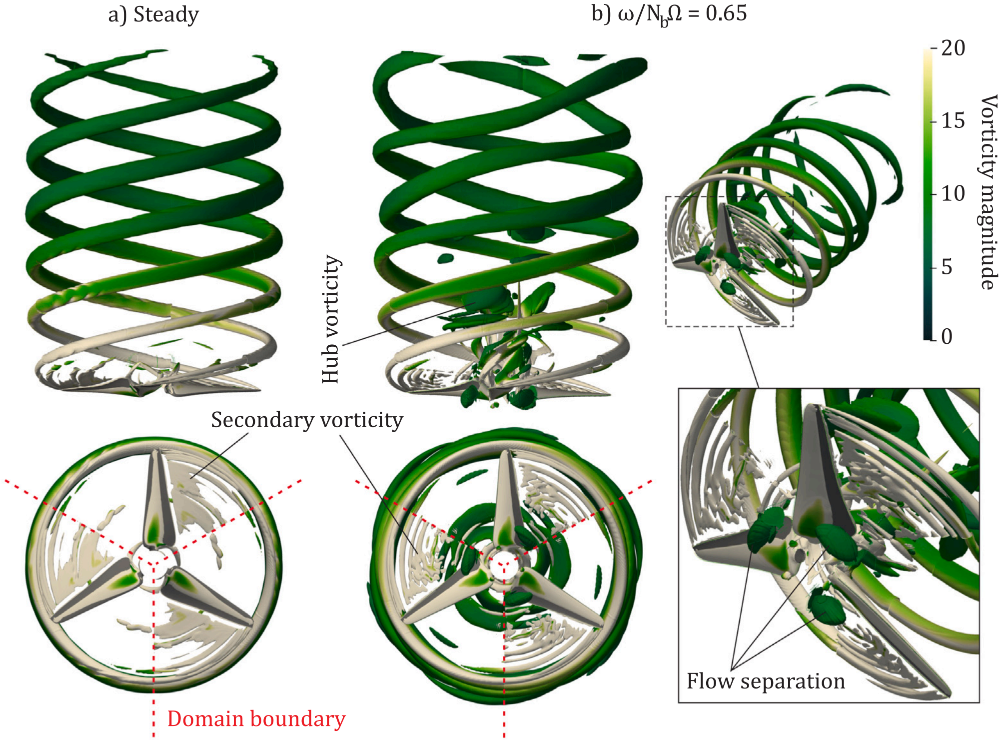

Fig. 5. 3D wake vorticity obtained from URANS simulations using the Q-criterion. (a) Steady flow, (b) unsteady flow at $\omega/N_b\Omega = 0.65$.

4.2.2. Load cycles and mean performance

Fig. 6a shows typical load cycles for a single gust period for three selected URANS cases. The solid lines represent the thrust coefficient (Eq. (15)) while the dotted lines represent power coefficient (Eq. (16)). The three cases were selected as representative of low, intermediate and high frequency cases ($\omega/N_b\Omega = 0.15,\ 0.42$ and 0.92 respectively). Horizontal lines indicating the steady power and thrust coefficients are included for reference.

The incoming gust amplitude is the same for all cases in Fig. 6a ($\epsilon = 0.15$), and the time on the x-axis has been normalised by the gust period. The unsteady load amplitude can be seen to differ between the three frequency cases, such that the largest amplitude response occurs at the intermediate frequency for both thrust and power. A notable difference between the cases in Fig. 6a is in the mean power and thrust coefficients: the highest frequency ratio (shown in blue) has higher mean loads than the other cases. This is illustrated more clearly in Fig. 6b, which shows the mean unsteady power and thrust coefficients for all simulated cases. Certain cases were simulated at half the gust amplitude, to check for amplitude-dependence: cross markers indicate an amplitude of $\epsilon = 0.15$, while circles indicate $\epsilon = 0.075$. Blue markers show the mean thrust coefficient while red markers show the mean power coefficients. Horizontal lines indicate the steady-flow values from Fig. 4b.

The mean loads in Fig. 6b increase with increasing frequency ratio. In particular, the power coefficient is notably higher than in steady flow. Increased mean power production has previously been observed in tidal turbines operating in unsteady high-turbulence flow (Gaurier et al., 2020a; Blackmore et al., 2016). Holst et al. (2015) also observed a gradual increase in mean turbine power in their CFD simulations of a tidal turbine operating in surface waves. It will be shown in Section 4.2.4 that in the present case the increased loads seen in the URANS simulations are due to an increase in the in-plane bending moment and thrust produced along the inner 50% of blade span in unsteady conditions. It is notable that the smaller-amplitude gusts produce a smaller increase in the mean power coefficients, and virtually no change to the mean thrust coefficient, suggesting that these effects are amplitude-dependent.

4.2.3. Load amplitude and phase

Trends in the load response with changing frequency ratio are more easily visualised by considering the load amplitude and phase separately. The thrust, power and out-of-plane bending moment coefficient amplitudes are defined as:

$$|C_T'| = \frac{T_{cycle,\ max} - T_{cycle,\ min}}{\rho U_\infty^2 S} \tag{20}$$

$$|C_P'| = \frac{(Q_{cycle,\ max} - Q_{cycle,\ min})\Omega}{\rho U_\infty^3 S} \tag{21}$$

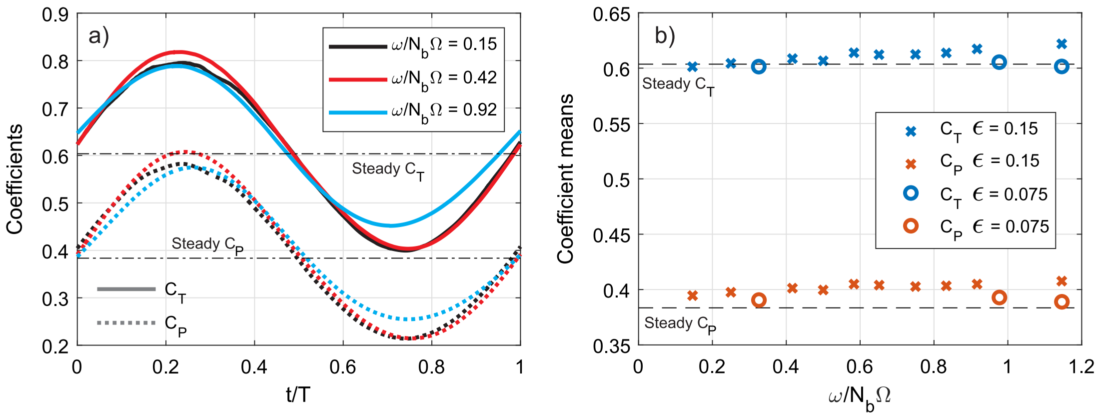

Fig. 6. (a) Variation of turbine thrust and power coefficients over a single fully-developed gust cycle from the URANS simulations, at three representative inflow frequencies. (b) Mean thrust and power coefficients as obtained from the URANS simulations. (For interpretation of the references to colour in this figure legend, the reader is referred to the web version of this article.)

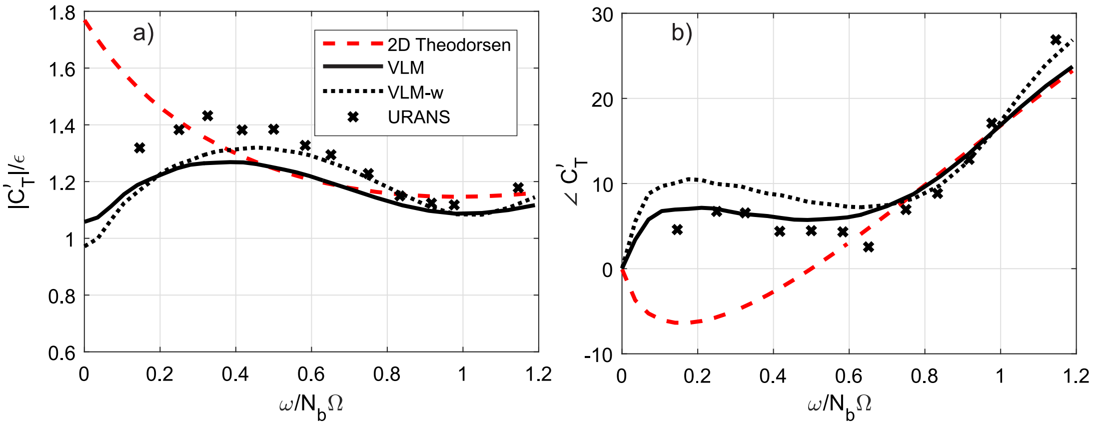

Fig. 7. (a) Amplitude and (b) phase of the unsteady thrust coefficient (Eq. (20)) as obtained from URANS, VLM and the 2D Theodorsen function.

$$|C_M'| = \frac{(M_{f\ cycle,\ max} - M_{f\ cycle,\ min})}{\rho U_\infty^2 S R} \tag{22}$$

where M_f is the total out-of-plane (flapwise) bending moment. These coefficients represent half of the peak-to-peak values of a single fully-developed load cycle, such as the ones shown in Fig. 6a. The results below are further normalised by the non-dimensional gust amplitude ϵ (see Eq. (13)). This normalisation of the unsteady flow results was identified by Sequeira and Miller (2014) as enabling consistent comparison between different gust amplitudes when simulating tidal turbine gust interaction. The phase (denoted $\angle C_T'$, $\angle C_P'$ and $\angle C_M'$) is more challenging to obtain since the URANS results are not perfectly sinusoidal. The phase results shown below were obtained by taking the average value of the two zero-crossings of a single load cycle.

Fig. 7a and b respectively show the amplitude and phase of the unsteady thrust response of the turbine against frequency ratio. The cross markers represent URANS results. The solid and dotted black lines denote VLM (fixed wake) and VLM-w (quasi-free wake, see Section 3.1) respectively, while the red dashed line gives the prediction by the 2D Theodorsen function (obtained using the method described in Section 3.3).

In general, Fig. 7 shows that the agreement with the URANS is closer for the VLM than for Theodorsen's function. Looking first at the unsteady thrust amplitude in Fig. 7a, at quasi-steady frequencies (frequency ratios near zero) the 2D amplitude is significantly higher than the 3D simulations, which is expected due to the lack of tip-loss corrections. However, as the frequency ratio increases, the 2D predictions approach the 3D results, such that from about $\omega/N_b\Omega = 0.7$ the amplitudes of all models are similar. This can be explained by the diminishing effects of the streamwise wake vorticity (which includes the tip vortices), as demonstrated by Smyth et al. (2021): streamwise wake effects diminish with increasing forcing frequency, meaning that the associated wake downwash is diminished. This means that at high frequencies the unsteady load response approaches the 2D result, despite significant 3D features in the geometry. A similar trend can be seen in the phase in Fig. 7b: the 2D and 3D phases differ significantly at lower frequencies, with the 3D phase response leading the gust forcing while the 2D function predicts a phase lag. However, from about $\omega/N_b\Omega = 0.6$ the 2D and 3D phase responses show good agreement. These frequency-dependent trends in the integrated loads are explained by

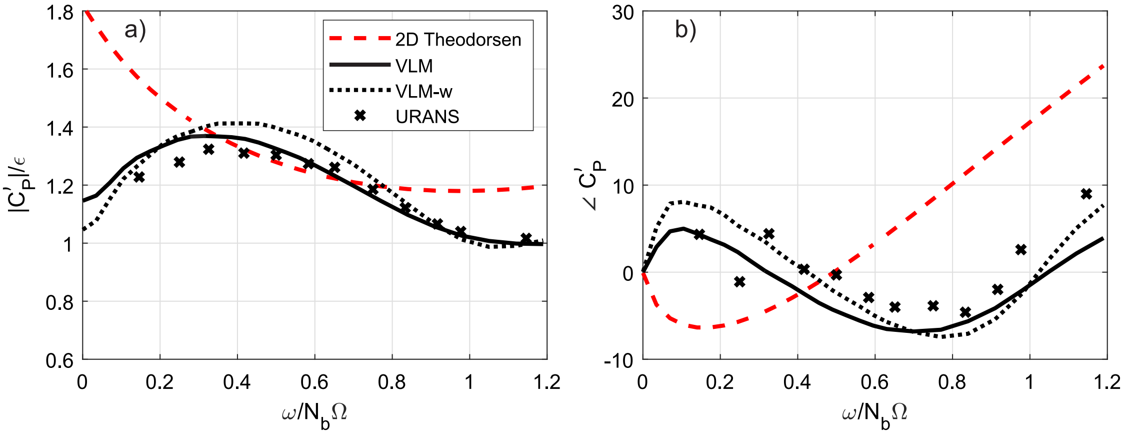

Fig. 8. (a) Amplitude and (b) phase of the unsteady power coefficient (Eq. (21)) as obtained from URANS, VLM and the 2D Theodorsen function.

the diminishing downwash from streamwise wake vorticity with increasing forcing frequency (Smyth et al., 2021), which is captured by the VLM but not by the 2D Theodorsen function. As such the two methods are in closer agreement at high gust frequencies but differ at low frequencies.

The VLM under-predicts the thrust amplitude at lower frequency ratios by up to around 10%, but agrees better at the higher frequencies, and follows the same trend as the URANS results: the maximum thrust amplitudes in both URANS and VLM occur at frequency ratio of $\omega/N_b\Omega \approx 0.4$. Based on the analysis in Section 2.3, using Eq. (8) we can estimate the peak load frequency ratio: using $n = 0$ and $\Delta\Phi = 0.3$, and the mid-span reduced frequency from Table 1 ($k = 0.24$) we obtain $(\omega/N_b\Omega)_{peak} \approx 0.38$. Thus Eq. (8) is able to predict the frequency ratio of maximum load amplitude with reasonable accuracy, and the load amplitude peak at $(\omega/N_b\Omega)_{peak} \approx 0.4$ is likely due to returning wake effects as introduced in Section 2.3. The peak amplitude is about 20%–35% higher than the quasi-steady amplitude at $\omega/N_b\Omega = 0$. It is often assumed in tidal turbine modelling that a quasi-steady flow assumption is conservative with respect to loads, but Fig. 7a demonstrates that this is not the case for this geometry and flow configuration.

Similar trends can be found in the unsteady load amplitude and phase of the power coefficient, shown in Fig. 8. The peak amplitudes of the 3D simulations in Fig. 8a also occur at frequency ratio ≈ 0.4, and are 20–40% higher than the quasi-steady amplitude. The 2D prediction is substantially higher than the 3D results at low frequencies, and decreases with increasing frequency ratio. By contrast, the 3D amplitudes initially increase with increasing frequency ratio. As such, the 2D and 3D results show completely different load trends. The VLM here predicts the load amplitude to within 5% of the URANS for the entire frequency range.

It is notable that unlike the thrust coefficient in Fig. 7, the 2D prediction of the unsteady power coefficient does not approach the 3D simulation results in Fig. 8. Fig. 8a shows good agreement in the amplitude at intermediate frequency ratios (about 0.3–0.8), but at higher frequencies the 2D prediction again deviates from the 3D results. Looking at the phase in Fig. 8b, the agreement between 2D and 3D results is poor at virtually all frequencies, and the trends are completely different. This may be because the turbine torque is more affected by tip effects: Smyth et al. (2021) demonstrated that near the tips of a finite wing or rotor, the downwash from streamwise wake vorticity remained high also at high gust frequencies and never approached the 2D result. As the power coefficient is more affected by tip effects than the thrust coefficient, this may explain why the 2D thrust coefficient in Fig. 7 approaches the 3D results with increasing frequency ratio, while the 2D power coefficient in Fig. 8 does not.

The unsteady out-of-plane bending moment coefficient amplitude and phase are shown in Fig. 9. The variation in amplitude with increasing frequency ratio in Fig. 9a is not as pronounced as for the thrust and power coefficient amplitudes above, but a shallow peak around $\omega/N_b\Omega \approx 0.4$ can still be observed. The peak load at this frequency predicted by VLM is about 15%–25% higher than the quasi-steady amplitude at $\omega/N_b\Omega = 0$. As for the thrust in Fig. 7, the 2D and 3D results differ at low frequency ratios, but the agreement in amplitude is better from $\omega/N_b\Omega \approx 0.4$, and the agreement in phase is better from $\omega/N_b\Omega \approx 0.8$.

Overall, the results in Figs. 7–9 show that the 3D solvers (viscous CFD, and inviscid VLM/VLM-w) show similar trends in both unsteady load amplitude and phase. The amplitude predicted by VLM is consistently within 10% of the URANS results at low frequency ratios, and the agreement is within 5% in the majority of cases. This indicates that the leading-order cause of discrepancy between the Theodorsen function and the URANS results is the omission of streamwise wake vorticity in the unsteady wake (as discussed above and in Section 2.2), which is included in the VLM and gives rise to the trends seen, even though there is still some remaining discrepancy between VLM and URANS. The addition of a quasi-free wake (VLM-w) does not substantially improve the agreement with URANS. Finally, the 2D function generally gives conservative load estimates, but only if no tip-loss corrections are added (see Section 4.3).

4.2.4. *Spanwise load distributions*

Fig. 10 shows the spanwise load distributions for two frequency cases: $\omega/N_b\Omega = 0.42$ (Fig. 10a and c) and 0.92 (Fig. 10b and d). The former represents a low-frequency case, and is also the frequency resulting in the highest overall load amplitude. The latter represents a high-frequency case.

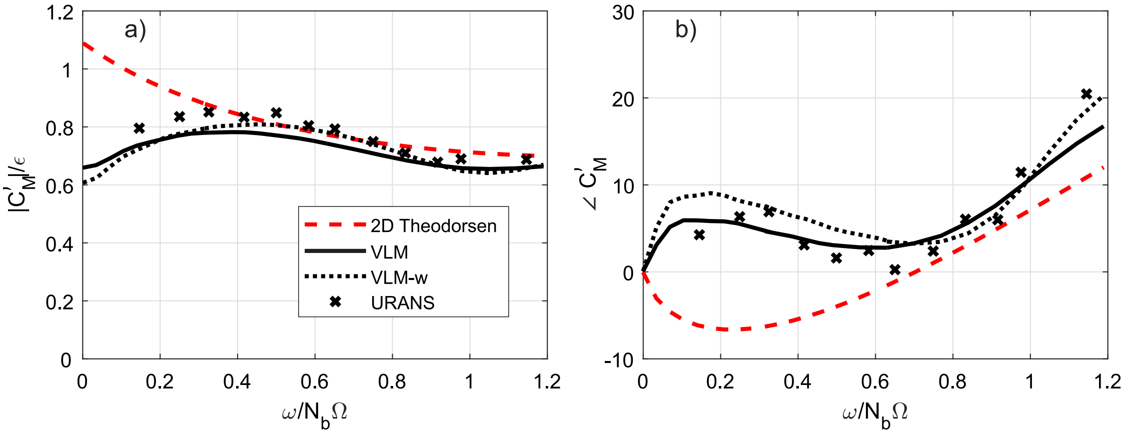

Fig. 9. (a) Amplitude and (b) phase of the unsteady out-of-plane bending moment coefficient (Eq. (22)) as obtained from URANS, VLM and the 2D Theodorsen function.

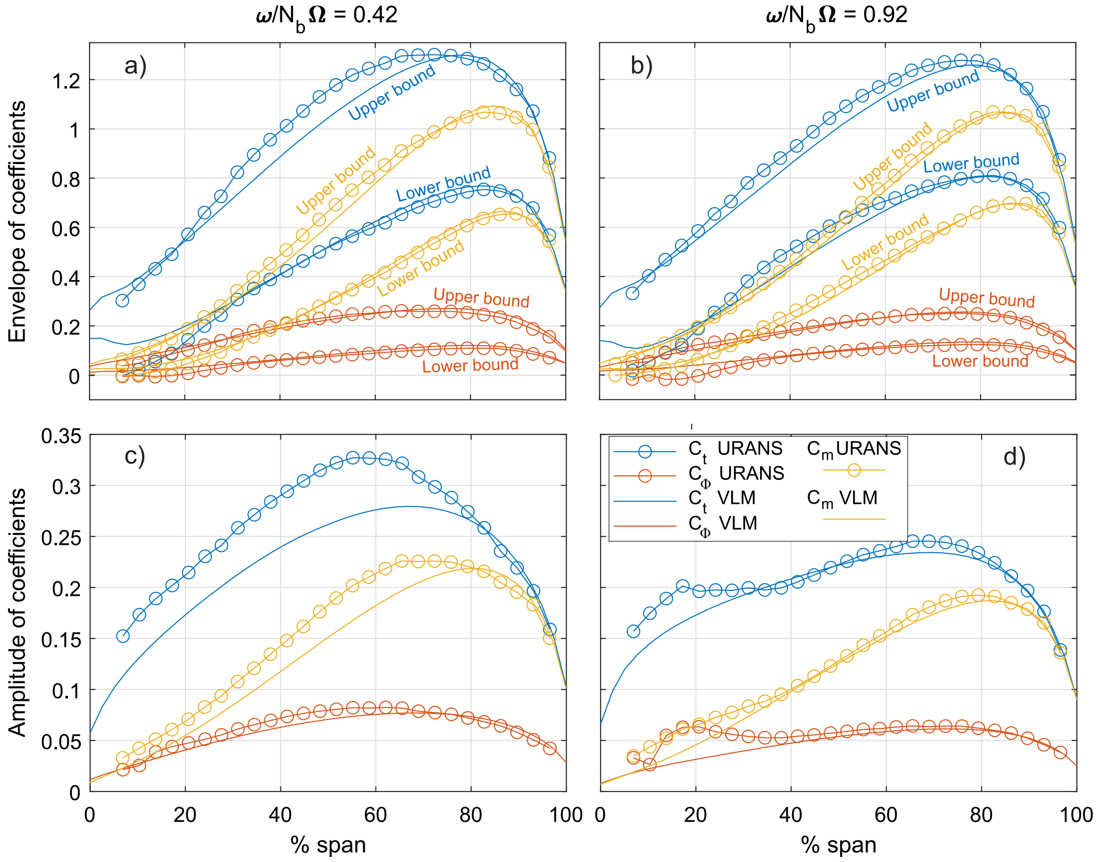

Fig. 10. Spanwise distributions of the unsteady loads per unit span, for two representative frequencies. Envelope of thrust and bending moment coefficients for (a) frequency ratio 0.42 and (b) frequency ratio 0.92. Local amplitude of the unsteady thrust and bending moment coefficients for (c) frequency ratio 0.42 and (d) frequency ratio 0.92. (For interpretation of the references to colour in this figure legend, the reader is referred to the web version of this article.)

Fig. 10a and b show the envelope of the thrust and moment coefficients during one gust cycle, indicating the highest and lowest value recorded at each spanwise position. Fig. 10c and d show the amplitude of the unsteady loading at each spanwise position, given by half of the peak-to-peak magnitude.

Looking at the load envelopes in Fig. 10a and b, the VLM shows good agreement with URANS along much of the span for both frequencies. The improvement is notable compared to the steady-state loading seen in Fig. 4b, where the VLM over-predicts the loads

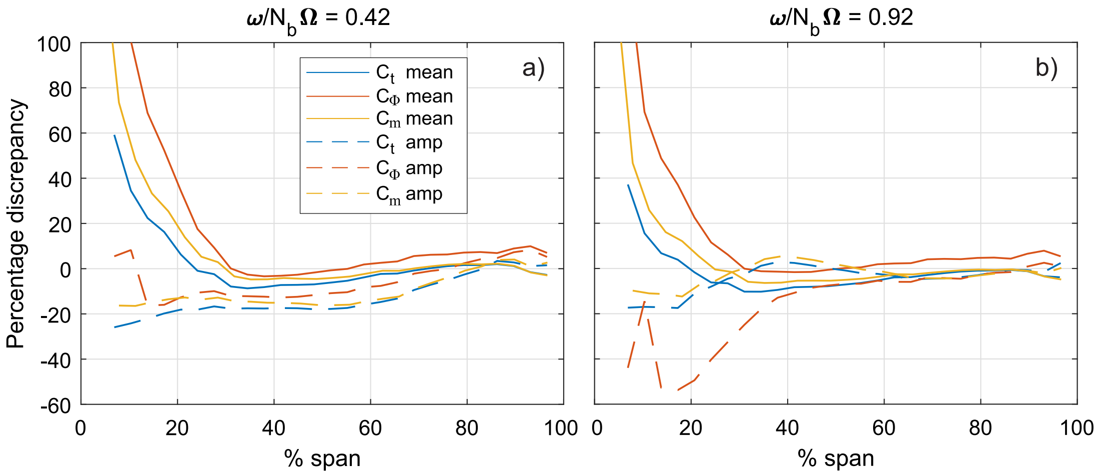

Fig. 11. Percentage discrepancy in the spanwise mean loads and load amplitudes as predicted by VLM compared to URANS, for frequency ratios (a) 0.42 and (b) 0.92. (For interpretation of the references to colour in this figure legend, the reader is referred to the web version of this article.)

in the innermost 50% of the span. In Fig. 10a and b the agreement in this spanwise region is significantly improved, especially in the case of the in-plane moment coefficient C_{Φ}. The upper bound of the thrust coefficient envelope is slightly under-predicted by the VLM along the mid-span at the lower frequency in Fig. 10a, which explains the under-prediction of the thrust amplitude by the VLM in Fig. 7a relative to URANS at this frequency. For the higher frequency in Fig. 10b both the upper and lower bounds of the thrust envelope are slightly under-predicted by the VLM relative to URANS.

Looking at the spanwise load amplitudes in Fig. 10c and d, at the lower frequency the unsteady thrust amplitude is under-predicted by the VLM relative to URANS over the innermost 70% of the span, due to the under-prediction of the upper bound in Fig. 10a. However, this results in only 10% discrepancy in the total load amplitude in Fig. 7a, making it acceptable for a first-order estimate of the unsteady loads. Looking at the higher frequency in Fig. 10d, the unsteady amplitude is well predicted along the whole span for both thrust and bending moments, except for a deviation around 20% span. The relative amplitude of the incoming gust is high in this area (see Table 1) which may contribute to nonlinear effects and stall in the URANS simulations. Furthermore, the differences in model representation of the hub region may contribute to discrepancies, since the URANS centre boundary is an inviscid wall while the VLM effectively has an open centre.

The agreement between VLM and URANS predictions for these frequency ratios can be seen more clearly in Fig. 11, which shows the mean load and load amplitude percentage discrepancies in VLM compared to URANS, for the same frequencies as in Fig. 10. Looking at the errors in the mean loads (solid lines), both frequencies show similar trends: thrust and out-of-plane bending moment coefficients are within 10% outboard of 10%–20% span, while in-plane bending moment coefficients are within 10% outboard of about 25% span. This is in contrast to the steady flow results in Fig. 4d, which showed the VLM to agree with RANS to within 10% only on the outer 50% of the blade span. This means that the mean spanwise loads predicted by VLM agree better with URANS in the unsteady flow conditions, and the improvement occurs over the inboard blade sections. Fig. 11 also shows the errors in unsteady load amplitude (dashed lines). It can be seen that the high frequency case (Fig. 11b) has lower errors over the outboard part of the span, while the low frequency case (Fig. 11a) has lower errors near the hub. As stated in Section 4.1, the absolute loads are small in the hub region and so this inflates the percentage errors. As such, the discrepancies in the inboard sections have only small effect on the overall thrust and power coefficient amplitudes, as seen in Figs. 7–9. Because of this, the VLM still offers good predictive unsteady load capabilities relative to URANS.

4.3. Quasi-steady tip-loss corrections in unsteady flow

As discussed in Section 1 and Section 2, the industry-standard method for modelling unsteady blade loading is Blade Element Momentum Theory (BEM). The effect of proximity to the blade tip is usually accounted for in BEM through tip-loss corrections, which generally assume quasi-steady flow. However, as discussed in Sections 1 and 4.2.3, in unsteady flow conditions tip-loss effects caused by the 3D wake downwash are diminished, such that the overall loads approach those of 2D flows with increasing reduced frequency (Smyth et al., 2021). This suggests that the application of conventional quasi-steady tip-loss corrections may be inappropriate for evaluating unsteady loads. This is illustrated in Fig. 12 for the model turbine and flow conditions used in this paper. Fig. 12a, b and c respectively show the amplitudes of the unsteady thrust, power and out-of-plane bending moment coefficients, as predicted by the VLM (solid black lines) and by the 2D Theodorsen function with and without a quasi-steady tip-loss correction applied (dotted and dashed red lines respectively). The tip-loss corrected result is obtained by extracting the quasi-steady sectional lift coefficients from the VLM at $\omega/N_b\Omega = 0$, and subsequently applying the Theodorsen function as a modifier to the lift at each section (see Section 3.3). This gives the tip-loss exactly as predicted by quasi-steady VLM, which is then assumed to be constant with

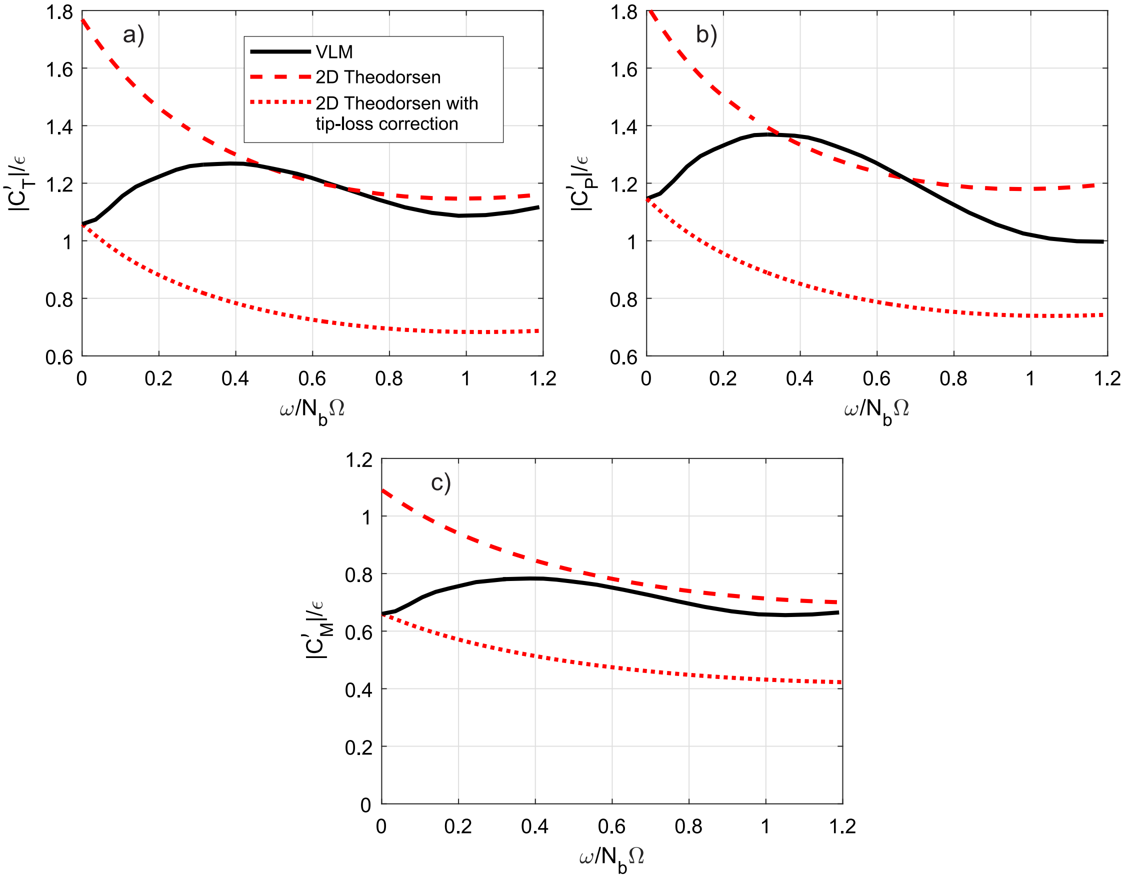

Fig. 12. Unsteady load amplitudes resulting from oscillatory inflow velocity, as obtained by 3D VLM, the 2D Theodorsen function, and the Theodorsen function corrected to account for quasi-steady tip-loss effects. (a) Unsteady thrust coefficient amplitude, (b) unsteady power coefficient amplitude, (c) unsteady out-of-plane moment coefficient amplitude.

increasing gust frequency, in line with the approach of many BEM codes. Note that the 3D VLM accounts for the tip loss directly, through the downwash induced by the turbine wake.

The uncorrected 2D function in Fig. 12 is conservative throughout most of the frequency range. Quasi-steady tip effects works to reduce turbine loads, and so at low frequencies the uncorrected 2D function substantially over-predicts both the thrust and power amplitudes. By contrast, the corrected 2D function severely under-predicts the unsteady load amplitude throughout the whole frequency range. At $\omega/N_b\Omega = 0.4$ the corrected 2D function under-predicts both the power and thrust coefficient amplitudes by over 60% relative to the 3D result, and the out-of-plane bending moment by over 30%. A quasi-steady load assumption (using the load response at $\omega/N_b\Omega = 0$) would under-predict loads by 15-20% compared to the 3D unsteady results at this frequency. Notably, Milne (2014) found that a dynamic inflow model without tip-loss correction over-predicted the unsteady load amplitude of an experimental model turbine in oscillatory movement, while a model that included a tip-loss correction under-predicted the load. A similar conclusion can be drawn from Fig. 12, and the discrepancy is here caused by the frequency-dependence in the streamwise wake downwash effects which is captured by VLM but not by the 2D models (Smyth et al., 2021).

5. Realistic frequency ratios

5.1. Site measurements of surface waves

The results above indicate a critical frequency ratio of 0.4 at which there is a peak in the normalised load amplitude, of the order of 20%–40% higher than the quasi-steady load amplitude which is often assumed to represent peak load conditions. To determine the practical implications of this finding, it is important to determine whether this frequency ratio is likely to occur for full-scale turbines in realistic flow conditions. In this section, we briefly investigate the likelihood of a utility-scale turbine operating at the peak load frequency ratio.

While this study uses an idealised inflow gust profile to investigate the hydrodynamic response and evaluate the applicability of 2D modelling, the gust is similar to that seen by a turbine operating in long-period surface waves. As such, the conclusions drawn

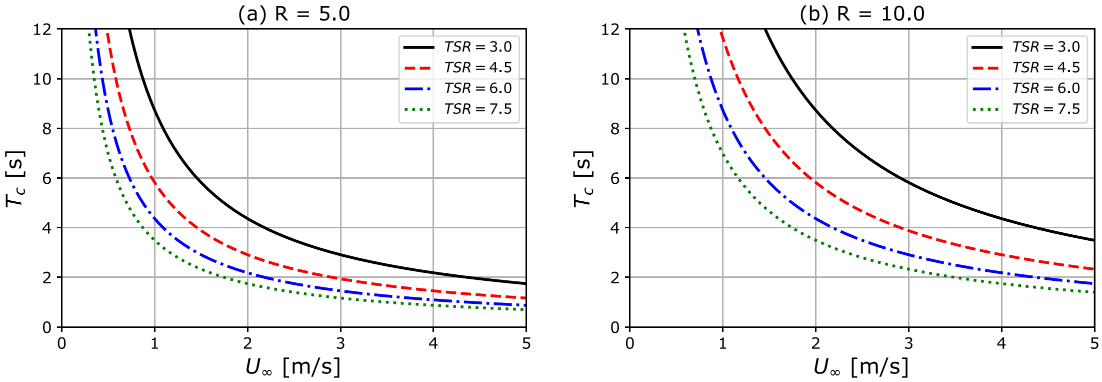

Fig. 13. Critical forcing period T_c expressed as a function of tip-speed ratio and inflow speed for a three-bladed turbine at two different rotor diameters.

are relevant to this class of unsteady flow. Using the likely range of reduced frequencies experienced by a tidal turbine in waves as evaluated by Sequeira and Miller (2014), Eq. (8) suggests that a critical frequency ratio of $\omega/N_b\Omega = 0.4$ (as was identified for the model turbine above) is likely to be a good approximation for the peak load frequency ratio of most turbine blade geometries.

The frequency ratio in a given wave state is determined by the wave period T, since it is related to the forcing frequency as $T = 2\pi/\omega$. It is convenient to introduce a critical forcing period T_c corresponding to the wave period resulting in a frequency ratio of 0.4 for a given inflow speed and turbine geometry. Rearranging Eq. (7), T_c is then given by:

$$T_c = \frac{2\pi}{0.4 N_b \Omega} \tag{23}$$

where the turbine rotational frequency Ω is determined by the inflow speed U_∞, the blade radius and the TSR. Fig. 13a shows T_c against U_∞ for a 3-bladed rotor of 5-metre radius, and Fig. 13b the same for 10-metre radius, for different TSRs. The range of U_∞ has been chosen to encompass flow speeds at typical tidal power sites. It can be seen that increasing TSR or U_∞ reduces the critical wave period, while increasing the turbine diameter increases the critical wave period.

The results in Fig. 13 show critical periods that are generally between 2 and 10 s for flow speeds of 1 to 3 m/s. These periods are comparable to typical sea states at sites that are of interest for the development of tidal stream energy. Mullings et al. (2023), for example, reported measured wave periods between 3 and 8 s in Raz Blanchard. Filipot et al. (2015) showed typical periods around 10 s for Paimpol Bréhat, but with some swell-dominated sea states with waves of up to 20-s periods. Sellar et al. (2018) measured peak spectral periods from approximately 3 to 13 s at the Fall of Warness. The ranges of periods in these examples, for different sites, fall within some of the conditions observed in Fig. 13. This analysis suggests that for a typical turbine at a typical site, the wave conditions are likely to coincide with the frequency ratio that gives the largest unsteady load amplitudes relative to the wave height.

5.2. *Frequency ratios from literature*

As has been established above, a turbine operating at a typical tidal power site is likely to experience wave-induced loading at the critical frequency ratio. Therefore, it is important to carry out experimental studies to understand turbine loading under these conditions. Many experimental studies have been carried out on the response of model-scale tidal turbines to the combined effects of currents and waves. Table 2 presents a summary of 13 experimental campaigns performed in both flumes (F) and towing tanks (TT). The table summarises rotor diameter, inflow speed, range of rotational frequencies, range of wave frequencies, number of blades, and the resulting range of frequency ratios identified for each study by the authors of the present paper.

At least six studies present frequency ratio ranges that include the critical value of 0.4 identified in this study, where peak wave-induced loads relative to the wave amplitude might be expected. Such frequency ratios, however, are normally attained through operation at lower than design TSR, meaning that stall is likely to occur over sections of the blade. This suggests that there is a need for experimental studies carried out at higher frequency ratios while keeping the turbine operating point at the design TSR, in order to verify the role of frequency ratio in determining wave-induced loads, and to represent realistic site conditions.

Conclusions

This paper has shown the load response of a model tidal turbine to small-amplitude harmonic gusts representative of long-period surface wave loading. High-order viscous modelling using unsteady Reynolds-Averaged Navier Stokes (URANS) simulations has been compared with low-order inviscid modelling using a 3D inviscid vortex lattice model (VLM) and predictions from the 2D Theodorsen function, which is commonly used in industrial turbine design tools. The results show that the 2D model captures neither the magnitude nor the trends in the load response. The 3D VLM does not capture viscous drag and thus substantially over-predicts

Table 2
Summary of experimental campaigns executed in flumes (F) and towing tanks (TT) to study the response of tidal turbines under the effects of surface waves. Wave frequencies are presented on a rotor-based reference frame.

Authors	D [m]	U_∞ [m/s]	Ω [rad/s]	ω [rad/s]	N_b	$\omega/N_b\Omega$
Barltrop et al. (2007) (TT)	0.40	0.00–1.20	6.70–15.71	3.33–8.59	3	0.07–0.43
Faudot and Dahlhaug (2012) (TT)	1.48	0.27, 0.67, 1.07	2.56–10.16	2.71–6.24	2	0.13–1.22
Gaurier et al. (2013) (F)	0.90	0.67, 0.68	1.49–11.91	3.14–4.40	3	0.09–0.98
Luznik et al. (2013) (TT)	0.46	0.60	10.96–18.26	4.29–4.29	3	0.08–0.13
Stallard et al. (2013) (F)	0.27	0.47	15.0	5.02[a]	3	0.11
Galloway et al. (2014) (TT)	0.80	0.90	9.00–16.88	2.64–6.77	3	0.05–0.25
de Jesus Henriques et al. (2014) (F)	0.50	0.50	7.00–14.70	3.04–4.42	3	0.07–0.21
Guo et al. (2018) (TT)	0.80	0.56–0.68	7.65–11.90	2.40–9.02	3	0.07–0.39
Martinez et al. (2018) (F)	1.20	0.77–0.81	5.73–10.00	2.09–3.14	3	0.07–0.18
Draycott et al. (2019) (F)	1.20	0.81	9.33	1.95–3.46	3	0.07–0.12
Ordonez-Sanchez et al. (2019) (TT)	0.83	1.00	3.14–7.96	4.15–6.30	3	0.17–0.67
Porter et al. (2020) (F)	0.83	0.80	4.71–11.52	3.14	3	0.09–0.22
Gaurier et al. (2020b) (F & TT)	0.724	0.80, 1.00	2.21–19.34	3.14–4.40	3	0.05–0.66
Zang et al. (2023) (F)	0.30	0.40	10.40	3.14–6.31	3	0.10–0.20
Watanabe et al. (2023) (TT)	0.40	0.60	5.00–17.50	5.07–11.79	3	0.10–0.79
McNaughton et al. (2025) (TT)	1.20	1.00	4.14–11.91	1.88–5.97	3	0.06–0.25

[a] Peak spectral frequency.

the steady power coefficient, however it shows better agreement in the thrust and out-of-plane bending moment coefficients, and the integrated unsteady load amplitudes are consistently within 10% of the URANS results, with the majority of cases being within 5%. The VLM also shows the same trends as URANS with regards to load amplitude and phase variation with increasing gust frequency. Spanwise load distributions indicate that discrepancy between VLM and URANS simulations primarily occur on the inboard sections of the blade, where viscous and nonlinear effects due to large angle of attack amplitudes are not captured by the VLM.

Taken together, the agreement in loads and trends between the VLM and the URANS and the differing trends in the 2D predictions indicate that the absence of streamwise wake vorticity downwash in the 2D function is responsible for its discrepancy with the 3D numerical results. It has been further shown that applying a quasi-steady tip-loss correction to the Theodorsen function resulted in under-prediction of the unsteady load amplitudes by 30%–60% relative to VLM.

The ‘frequency ratio’ $\omega/N_b\Omega$ has been identified as a significant indicator of the unsteady turbine loads, and the peak loads for the present turbine design and inflow conditions were observed to occur at a ratio of around 0.4. A simple analysis shows that this frequency ratio likely represents the peak unsteady load scenario (relative to gust amplitude) for most realistic tidal turbine designs. It was confirmed that this frequency ratio is likely to occur in typical surface wave site conditions for full-scale turbines, and so the 3D effects demonstrated in the present study may represent a peak-load scenario for industrial-scale turbines.

The outcomes of this study have implications for the peak and lifetime load evaluation of tidal turbines, and point to the need for 3D modelling tools for dynamic load evaluation on low aspect ratio rotors. There is also a need for further work in experimentally confirming the role of frequency ratio in identifying peak dynamic load conditions. Future work based on the outcomes of this study include improving the performance of the VLM by correcting for nonlinear and viscous effects, and creating a new frequency-dependent tip-loss correction to improve the applicability of the Theodorsen function for tidal rotors.

CRediT authorship contribution statement

Amanda S.M. Smyth: Writing – original draft, Software, Methodology, Conceptualization. **Federico Zilic de Arcos:** Writing – original draft, Methodology, Data curation. **Anna M. Young:** Writing – review & editing, Supervision, Conceptualization.

Declaration of competing interest

The authors declare that they have no known competing financial interests or personal relationships that could have appeared to influence the work reported in this paper.

Data availability

Data will be made available on request.

References

Adcock, T.A.A., Draper, S., Willden, R.H.J., Vogel, C.R., 2021. The fluid mechanics of tidal stream energy conversion. Annu. Rev. Fluid Mech. 53, 287–310.

Afgan, I., McNaughton, J., Rolfo, S., Apsley, D., Stallard, T., Stansby, P., 2013. Turbulent flow and loading on a tidal stream turbine by LES and RANS. Int. J. Heat Fluid Flow 43, 96–108.

Ahmed, U., Apsley, D., Afgan, I., Stallard, T., Stansby, P., 2017. Fluctuating loads on a tidal turbine due to velocity shear and turbulence: Comparison of CFD with field data. Renew. Energy 112, 235–246. http://dx.doi.org/10.1016/j.renene.2017.05.048.

Apsley, D.D., Stallard, T., Stansby, P.K., 2018. Actuator-line CFD modelling of tidal-stream turbines in arrays. J. Ocean. Eng. Mar. Energy 4, 259–271.

Apsley, D., Stansby, P., 2020. Unsteady thrust on an oscillating wind turbine: Comparison of blade-element momentum theory with actuator-line CFD. J. Fluids Struct. 98, 103141.

Ayancik, F., Zhong, Q., Quinn, D.B., Brandes, A., Bart-Smith, H., Moored, K.W., 2019. Scaling laws for the propulsive performance of three-dimensional pitching propulsors. J. Fluid Mech. 871, 1117–1138.

Barltrop, N., Varyani, K.S., Grant, A., Clelland, D., Pham, X.P., 2007. Investigation into wave-current interactions in marine current turbines. Proc. Inst. Mech. Eng. A: J. Power Energy 221 (2), 233–242.

Beddoes, T.S., 1993. A Third Generation Model for Unsteady Aerodynamics and Dynamic Stall. Technical Report, Westland Helicopters Limited.

Bex, C.C., Carlier, C., Fur, A., Pinon, G., Germain, G., Rivoalen, E., 2020. A stochastic method to account for the ambient turbulence in Lagrangian Vortex computations. Appl. Math. Model. 88, 38–54.

Blackmore, T., Myers, L.E., Bahaj, A.S., 2016. Effects of turbulence on tidal turbines: Implications to performance, blade loads, and condition monitoring. Int. J. Mar. Energy 14, 1–26.

de Jesus Henriques, T.A., Tedds, S.C., Botsari, A., Najafian, G., Hedges, T.S., Sutcliffe, C.J., Owen, I., Poole, R.J., 2014. The effects of wave–current interaction on the performance of a model horizontal axis tidal turbine. Int. J. Mar. Energy 8, 17–35.

Draycott, S., Payne, G., Steynor, J., Nambiar, A., Sellar, B., Venugopal, V., 2019. An experimental investigation into non-linear wave loading on horizontal axis tidal turbines. J. Fluids Struct. 84, 199–217.

Dufour, M.-A., Pinon, G., Rivoalen, E., Blondel, F., Germain, G., 2024. Development and validation of a lifting-line code associated with the vortex particle method software dorothy. Wind. Energy 27 (7), 633–666. http://dx.doi.org/10.1002/we.2905, arXiv:https://onlinelibrary.wiley.com/doi/pdf/10.1002/we.2905 URL https://onlinelibrary.wiley.com/doi/abs/10.1002/we.2905.

El Fajri, O., Bowman, J., Bhushan, S., Thompson, D., O'Doherty, T., 2022. Numerical study of the effect of tip-speed ratio on hydrokinetic turbine wake recovery. Renew. Energy 182, 725–750. http://dx.doi.org/10.1016/j.renene.2021.10.030.

Fagan, E., Jiang, Y., Kazemi, A., Goggins, J., 2019. Design and testing of a full-scale 2 MW tidal turbine blade. In: Proceedings of the 13th European Wave and Tidal Energy Conference.

Faudot, C., Dahlhaug, O.G., 2012. Prediction of wave loads on tidal turbine blades. Energy Procedia 20, 116–133. http://dx.doi.org/10.1016/j.egypro.2012.03.014.

Filipot, J.-F., Prevosto, M., Maisondieu, C., Le Boulluec, M., Thomson, J., 2015. Wave and turbulence measurements at a tidal energy site. In: 2015 IEEE/OES Eleveth Current, Waves and Turbulence Measurement. CWTM, IEEE, pp. 1–9.

Galloway, P.W., Myers, L.E., Bahaj, A.S., 2014. Quantifying wave and yaw effects on a scale tidal stream turbine. Renew. Energy 63, 297–307.

Gaurier, B., Carlier, C., Germain, G., Pinon, G., Rivoalen, E., 2020a. Three tidal turbines in interaction: An experimental study of turbulence intensity effects on wakes and turbine performance. Renew. Energy 148, 1150–1164.

Gaurier, B., Davies, P., Deuff, A., Germain, G., 2013. Flume tank characterization of marine current turbine blade behaviour under current and wave loading. Renew. Energy 59, 1–12.

Gaurier, B., Ordonez-Sanchez, S., Facq, J.-V., Germain, G., Johnstone, C., Martinez, R., Salvatore, F., Santic, I., Davey, T., Old, C., et al., 2020b. MaRINET2 tidal energy round robin tests—performance comparison of a horizontal axis turbine subjected to combined wave and current conditions. J. Mar. Sci. Eng. 8 (6), 463.

Greco, L., Testa, C., 2021. Wind turbine unsteady aerodynamics and performance by a free-wake panel method. Renew. Energy 164, 444–459. http://dx.doi.org/10.1016/j.renene.2020.08.002.

Grondeau, M., Poirier, J.-C., Guillou, S., M'ear, Y., Mercier, P., Poizot, E., 2020. Modelling the wake of a tidal turbine with upstream turbulence: LBM-LES versus Navier-Stokes LES. Int. Mar. Energy J. 3 (2), 83–89. http://dx.doi.org/10.36688/imej.3.83-89, URL https://marineenergyjournal.org/imej/article/view/56.

Gu, J., Cai, F., Müller, N., Zhang, Y., Chen, H., 2020. Two-Way Fluid–Solid interaction analysis for a horizontal axis marine current turbine with LES. Water 12 (1), http://dx.doi.org/10.3390/w12010098.

Guo, X., Yang, J., Gao, Z., Moan, T., Lu, H., 2018. The surface wave effects on the performance and the loading of a tidal turbine. Ocean Eng. 156, 120–134.

Holst, M.A., Dahlhaug, O.G., Faudot, C., 2015. CFD analysis of wave-induced loads on tidal turbine blades. IEEE J. Ocean. Eng. 40 (3), 506–521. http://dx.doi.org/10.1109/JOE.2014.2331531.

Jahani, K., Langlois, R.G., Afagh, F.F., 2022. Structural dynamics of offshore wind turbines: A review. Ocean Eng. 251, 111136. http://dx.doi.org/10.1016/j.oceaneng.2022.111136.

Jones, A.R., Cetiner, O., Smith, M., 2022. Physics and modeling of large flow disturbances: Discrete gust encounters for modern air vehicles. Annu. Rev. Fluid Mech. 54, 469–493.

Jost, E., Klein, L., Leipprand, H., Lutz, T., Krämer, E., 2018. Extracting the angle of attack on rotor blades from CFD simulations. Wind. Energy 21 (10), 807–822. http://dx.doi.org/10.1002/we.2196.

Katz, J., Plotkin, A., 2001. Low-Speed Aerodynamics, vol. 13, Cambridge University Press.

Kinnas, S.A., Hsin, C., 2012. Boundary element method for the analysis of the unsteady flow around extreme propeller geometries. AIAA J. 30 (3), 688–696.

Leishman, J.G., Beddoes, T.S., 1989. A Semi-Empirical model for dynamic stall. J. Am. Helicopter Soc. 3 (34), 3–17.

Loewy, R.G., 1957. A Two-Dimensional approximation to the unsteady aerodynamics of rotary wings. J. Aeronaut. Sci. 24 (2), 81–92. http://dx.doi.org/10.2514/8.3777.

Lomele, M., Smyth, A.S., Chen, X., Willden, R.H., 2025. Aerodynamic damping assessment on wind turbine blades using 2D and 3D computational fluid dynamics. In: AIAA SCITECH 2025 Forum. http://dx.doi.org/10.2514/6.2025-1236.

Luznik, L., Flack, K.A., Lust, E.E., Taylor, K., 2013. The effect of surface waves on the performance characteristics of a model tidal turbine. Renew. Energy 58, 108–114.

Martinez, R., Payne, G.S., Bruce, T., 2018. The effects of oblique waves and currents on the loadings and performance of tidal turbines. Ocean Eng. 164, 55–64.

McCarthy, E., Cava, D.G., Martinez-Hergueta, F., Vogel, C., 2022. LoadTide – Final Report. Project Report, Supergen ORE Hub.

McNae, D., 2013. Unsteady Hydrodynamics of Tidal Stream Turbines (Ph.D. thesis). Imperial College London.

McNaughton, J., de Arcos, F.Z., Vogel, C., Willden, R., 2025. Dynamic loading of two side-by-side tidal stream turbines in regular waves. J. Fluids Struct. 133, 104259.

McNaughton, J., Rolfo, S., Apsley, D., Afgan, I., Stallard, T., Stansby, P., 2012. CFD prediction of turbulent flow on an experimental tidal stream turbine using RANS modelling. In: 1st Asian Wave and Tidal Energy Conference.

Menter, F.R., Kuntz, M., Langtry, R., 2003. Ten Years of Industrial Experience with the SST Turbulence Model. Turbul. Heat Mass Transf. 4 4, 625–632.

Milne, I.A., 2014. An Experimental Investigation of Turbulence and Unsteady Loading on Tidal Turbines (Ph.D. thesis). University of Auckland.

Milne, I., Day, A., Sharma, R., Flay, R., 2013. Blade loads on tidal turbines in planar oscillatory flow. Ocean Eng. 60, 163–174. http://dx.doi.org/10.1016/j.oceaneng.2012.12.027.

Moored, K.W., 2018. Unsteady three-dimensional boundary element method for self-propelled bio-inspired locomotion. Comput. Fluids 167, 324–340.

Moriarty, P.J., Hansen, A.C., 2005. AeroDyn Theory Manual. Technical Report, National Renewable Energy Lab., Golden, CO (US).

Mullings, H., Stallard, T., 2021. Assessment of dependency of unsteady onset flow and resultant tidal turbine fatigue loads on measurement position at a tidal site. Energies 14 (17), http://dx.doi.org/10.3390/en14175470.

Mullings, H., Stallard, T., Draycott, S., 2023. Turbine fatigue load prediction from field measurements of waves and turbulence. http://dx.doi.org/10.36688/ewtec-2023-390.

Mullings, H., Stallard, T., Payne, G., 2017. Operational Loads on a Tidal Turbine due to Environmental Conditions. In: Proceedings of the Twenty-Seventh International Ocean and Polar Engineering Conference. p. 939.

Ordonez-Sanchez, S., Allmark, M., Porter, K., Ellis, R., Lloyd, C., Santic, I., OD́oherty, T., Johnstone, C., 2019. Analysis of a horizontal-axis tidal turbine performance in the presence of regular and irregular waves using two control strategies. Energies 12 (3), 367.

Ouro, P., Nishino, T., 2021. Performance and wake characteristics of tidal turbines in an infinitely large array. J. Fluid Mech. 925, A30.

Pinon, G., Mycek, P., Germain, G., Rivoalen, E., 2012. Numerical simulation of the wake of marine current turbines with a particle method. Renew. Energy 46, 111–126.

Porter, K.E., Ordonez-Sanchez, S.E., Murray, R.E., Allmark, M., Johnstone, C.M., OD́oherty, T., Mason-Jones, A., Doman, D.A., Pegg, M.J., 2020. Flume testing of passively adaptive composite tidal turbine blades under combined wave and current loading. J. Fluids Struct. 93, 102825.

Posa, A., Broglia, R., Balaras, E., 2021. Instability of the tip vortices shed by an axial-flow turbine in uniform flow. J. Fluid Mech. 920, A19. http://dx.doi.org/10.1017/jfm.2021.433.

Posa, A., Viola, I.M., Broglia, R., 2024. Influence of the tip speed ratio on the wake dynamics and recovery of axial-flow turbines. Phys. Fluids 36 (5), 055109. http://dx.doi.org/10.1063/5.0203285.

Prandtl, L., 1921. Applications of modern hydrodynamics to aeronautics. US Gov. Print. Off..

Richez, F., 2018. Analysis of dynamic stall mechanisms in Helicopter Rotor environment. J. Am. Helicopter Soc. 63 (2), 1–11.

Scarlett, G.T., Sellar, B., van den Bremer, T., Viola, I.M., 2019. Unsteady hydrodynamics of a full-scale tidal turbine operating in large wave conditions. Renew. Energy 143, 199–213. http://dx.doi.org/10.1016/j.renene.2019.04.123.

Scarlett, G.T., Viola, I.M., 2020. Unsteady hydrodynamics of tidal turbine blades. Renew. Energy 146, 843–855.

Schepers, J.G., Heijdra, J., Foussekis, D., Øye, S., Rawlinson Smith, R., Belessis, M., Thomsen, K., Larsen, T., Kraan, I., Visser, B., Ganander, H., Carlen, I., Voutsinas, S., Belessis, M., Drost, L., 2002. Verification of European wind turbine design codes, VEWTDC; final report. Neth. Energy Res. Found. ECN.

Schluntz, J., Willden, R.H.J., 2015. The effect of blockage on tidal turbine rotor design and performance. Renew. Energy 81, 432–441.

Sellar, B.G., Wakelam, G., Sutherland, D.R., Ingram, D.M., Venugopal, V., 2018. Characterisation of tidal flows at the european marine energy centre in the absence of ocean waves. Energies 11 (1), 176.

Sequeira, C.L., Miller, R.J., 2014. Unsteady gust response of tidal stream turbines. In: 2014 Oceans - St. John's. pp. 1–10. http://dx.doi.org/10.1109/OCEANS.2014.7003026.

Shen, W.Z., Zhang, J.H., Sørensen, J.N., 2009. The Actuator Surface Model: A new Navier–Stokes based model for rotor computations. J. Sol. Energy Eng. 131 (1), 011002. http://dx.doi.org/10.1115/1.3027502, arXiv:https://asmedigitalcollection.asme.org/solarenergyengineering/article-pdf/131/1/011002/5714048/011002_1.pdf.

Slama, M., Pinon, G., El Hadi, C., Togneri, M., t Gaurier, B., Germain, G., Facq, J.-V., Nuño, J., Mansilla, P., Nicolas, E., Marcille, J., Pacheco, A., 2021. Turbine design dependency to turbulence: An experimental study of three scaled tidal turbines. Ocean Eng. 234, 109035. http://dx.doi.org/10.1016/j.oceaneng.2021.109035.

Smyth, A.S.M., 2020. Three-Dimensional Unsteady Hydrodynamics of Tidal Turbines (Thesis). University of Cambridge.

Smyth, A.S.M., Nishino, T., Young, A.M., 2023. Instabilities in tidal turbine wakes. In: Proceedings of the European Wave and Tidal Energy Conference. http://dx.doi.org/10.36688/ewtec-2023-454.

Smyth, A.S.M., Young, A.M., 2019. Three-dimensional unsteady hydrodynamic modelling of tidal turbines. In: Proceedings of the European Wave and Tidal Energy Conference: 13th EWTEC. p. 40077.

Smyth, A.S.M., Young, A.M., Di Mare, L., 2019. The effect of 3D geometry on unsteady gust response, using a vortex lattice model. In: AIAA SciTech Forum.

Smyth, A.S.M., Young, A.M., Di Mare, L., 2021. Effect of Three-Dimensional geometry on harmonic Gust–Airfoil interaction. AIAA J. 59 (2), 737–750.

Sørensen, J.N., Shen, W.Z., 2002. Numerical modeling of wind turbine wakes. J. Fluids Eng. 124 (2), 393–399.

Stallard, T., Collings, R., Feng, T., Whelan, J., 2013. Interactions between tidal turbine wakes: experimental study of a group of three-bladed rotors. Philos. Trans. R. Soc. A: Math. Phys. Eng. Sci. 371 (1985), 20120159. http://dx.doi.org/10.1098/rsta.2012.0159.

Theodorsen, T., 1935. General Theory of Aerodynamic Instability and the Mechanism of Flutter. NACA Technical Report No. 496.

Turnock, S., 1993. Prediction of Ship Rudder-Propeller Interaction Using Parallel Computations and Wind Tunnel Measurements (Ph.D. thesis). University of Southampton, URL https://eprints.soton.ac.uk/48365/.

Veers, P., Bottasso, C.L., Manuel, L., Naughton, J., Pao, L., Paquette, J., Robertson, A., Robinson, M., Ananthan, S., Barlas, T., Bianchini, A., Bredmose, H., Horcas, S.G., Keller, J., Madsen, H.A., Manwell, J., Moriarty, P., Nolet, S., Rinker, J., 2023. Grand challenges in the design, manufacture, and operation of future wind turbine systems. Wind. Energy Sci. 8 (7), 1071–1131. http://dx.doi.org/10.5194/wes-8-1071-2023.

Visbal, M., Yilmaz, T.O., Rockwell, D., 2013. Three-dimensional vortex formation on a heaving low-aspect-ratio wing: Computations and experiments. J. Fluids Struct. 38, 58–76. http://dx.doi.org/10.1016/j.jfluidstructs.2012.12.005.

Walker, S., Thies, P., 2021. A review of component and system reliability in tidal turbine deployments. Renew. Sustain. Energy Rev. 151, 111495. http://dx.doi.org/10.1016/j.rser.2021.111495.

Wang, L., Liu, X., Kolios, A., 2016. State of the art in the aeroelasticity of wind turbine blades: Aeroelastic modelling. Renew. Sustain. Energy Rev. 64, 195–210. http://dx.doi.org/10.1016/j.rser.2016.06.007.

Watanabe, S., Kamra, M.M., Hu, C., 2023. An experimental study of surface wave effects on two interacting tidal turbines. J. Mar. Sci. Technol. 1–12.

Whelan, J.I., Graham, J.M.R., Peiro, J., 2009. Inertia effects on horizontal axis tidal-stream turbines. In: Proceedings of the 8th European Wave and Tidal Energy Conference. EWTEC.

Wild, O., Gementzopoulos, A., Jones, A.R., 2024. Navigating unsteady airwakes: Three-dimensionality and sideslip in strong transverse gust encounters. In: AIAA SciTech Forum.

Wimshurst, A., 2018. Tip Flow Corrections for Horizontal Axis Wind and Tidal Turbine Rotors (Ph.D. thesis). University of Oxford.

Wimshurst, A., Willden, R.H.J., 2017. Analysis of a tip correction factor for horizontal axis turbines. Wind. Energy 20 (9), 1515–1528.

Wimshurst, A., Willden, R.H.J., 2018. Computational observations of the tip loss mechanism experienced by horizontal axis rotors. Wind. Energy 21 (7), 544–557.

Winter, A.I., 2011. Differences in fundamental design drivers for wind and tidal turbines. In: OCEANS 2011 IEEE - Spain. pp. 1–10. http://dx.doi.org/10.1109/Oceans-Spain.2011.6003647.

Young, A.M., Farman, J., Miller, R., 2016. Load alleviation technology for extending life in tidal turbines. pp. 521–530. http://dx.doi.org/10.1201/9781315229256-63.

Young, A.M., Smyth, A.S.M., 2021. Gust–Airfoil coupling with a loaded airfoil. AIAA J. 59 (3), 773–785. http://dx.doi.org/10.2514/1.J059688.

Zang, W., Zhang, Y., Zheng, Y., Zhang, J., Guan, D., Fernandez-Rodriguez, E., 2023. On the impact of waves and turbulence on the power fluctuations and wake structure of a tidal-stream turbine. Phys. Fluids 35 (5), 055115. http://dx.doi.org/10.1063/5.0142872.

Zilic de Arcos, F., Vogel, C., Willden, R., 2020. Extracting angles of attack from blade-resolved rotor CFD simulations. Wind. Energy 23 (9), 1868–1885.